POLITECNICO
MILANO 1863

SCUOLA DI INGEGNERIA INDUSTRIALE
E DELL'INFORMAZIONE

Identification of bounded trajectories near Apophis during Earth flyby via Lagrangian descriptors

Tesi di Laurea Magistrale in
Space Engineering - Ingegneria spaziale

Author: **Tommaso Xompero**

Student ID: 249098
Advisor: Prof. Francesco Topputo
Co-advisors: Carmine Giordano, Lucia Francesca Civati
Academic Year: 2025-26

Abstract

Apophis flyby of the Earth provides a singular opportunity to study an asteroid under tidal deformation forces. To this end, the RAMSES mission, together with two CubeSats, is tasked to study Apophis surface and interior. Trajectory design in non-autonomous systems, such as Apophis at its Earth flyby, is challenging since it cannot rely on traditional periodic orbits.

In this work, Lagrangian descriptors are used to understand if bounded trajectories around Apophis exist across the close encounter with the Earth. This method works best for 2-dimensional search spaces, however trajectory design problems are inherently 6-dimensional. To account for this, a dimensionality reduction strategy is introduced, exploiting the geometry of the close encounter and symmetry properties of the augmented Hill problem. After introducing this strategy, additional parametrizations are introduced to consider several choices of planar grids to sample initial conditions. Due to the high number of trajectories that need to be considered, a GPU parallelization strategy is considered to efficiently propagate the various alternatives.

Bounded orbits are found, and they share similarities with characteristic orbits of the augmented Hill problem, such as resonant terminator orbits. Some sample trajectories are successfully applied to the Farinella case, one of the two CubeSats accompanying the main spacecraft of the RAMSES mission, considering its navigation constraints. The result furthermore confirms the capability of Lagrangian descriptors to divide the phase space into regions of qualitatively different motion.

Keywords: Lagrangian descriptors, Augmented Hill problem, Apophis, Bounded motion

Abstract in lingua italiana

Il flyby terrestre di Apophis offre un'opportunità unica per studiare un asteroide sottoposto a forze di deformazione mareale. A tal fine, la missione RAMSES, insieme a due CubeSat, ha il compito di studiare la superficie e l'interno di Apophis. La progettazione della traiettoria in sistemi non autonomi, come nel caso di Apophis durante il suo passaggio ravvicinato alla Terra, è complessa poiché non può fare affidamento sulle tradizionali orbite periodiche.

In questo lavoro, i descrittori Lagrangiani vengono utilizzati per determinare se esistano traiettorie confinate attorno ad Apophis durante l'incontro ravvicinato con la Terra. Questo metodo è ottimale per spazi di ricerca bidimensionali; tuttavia, i problemi di progettazione delle traiettorie sono intrinsecamente a sei dimensioni. Per ovviare a ciò, viene introdotta una strategia di riduzione della dimensionalità, sfruttando la geometria dell'incontro ravvicinato e le proprietà di simmetria del problema di Hill aumentato. Dopo aver presentato tale strategia, vengono introdotte ulteriori parametrizzazioni per considerare diverse opzioni di griglie planari da cui ottenere le condizioni iniziali. Dato l'elevato numero di traiettorie da analizzare, viene adottata una strategia di parallelizzazione su GPU per propagare efficientemente le varie alternative.

Vengono identificate orbite confinate che presentano analogie con le orbite caratteristiche del problema di Hill aumentato, come le resonant terminator orbit. Alcune traiettorie campione vengono applicate con successo al caso di Farinella, uno dei due CubeSat che accompagnano lo spacecraft principale della missione RAMSES, tenendo conto dei suoi constraints di navigazione. Il risultato conferma inoltre la capacità dei descrittori Lagrangiani di dividere lo spazio delle fasi in regioni con moti qualitativamente differenti.

Parole chiave: Descrittori Lagrangiani, Problema di Hill aumentato, Apophis, Moto confinato

Contents

1 | Introduction

1.1. Context

Near-Earth asteroids have become primary targets of space missions due to their high scientific value and accessibility. In addition to this, the use of CubeSats has increased in recent years, driven by their relatively lower cost and faster development. Consequently, missions to near-Earth asteroids began incorporating CubeSats to improve the scientific return of the exploration missions [15, 29].

A significant target among the near-Earth asteroids is (99942) Apophis. Discovered in 2004, initial calculations suggested a 2.7% probability of collision with the Earth in 2029. Successive measurements refined the trajectory, ruling out the possibility of an impact in April 13^{th}, 2029. Instead, the asteroid will perform a fly-by with the Earth, passing within the geostationary ring [18].

This event presents a unique opportunity to study the internal structure of the asteroid. As Apophis passes near the Earth, the planet's tidal torques are expected to induce significant changes in the spin state and surface alterations [3]. Monitoring these changes with ground and in-orbit measurements will provide valuable data on the asteroid's interior structure, which can greatly benefit planetary defense strategies [4].

Driven by these motivations, both the European Space Agency (ESA) and the National Aeronautics and Space Administration (NASA) are planning missions to this particular asteroid. The ESA mission, named Rapid Apophis Mission for Space Safety (RAMSES), is designed to carry two CubeSats to maximize scientific return [26]. NASA's strategy involves redirecting the OSIRIS-REx spacecraft toward Apophis, renaming the mission OSIRIS-APEX. Originally designed to sample the near-Earth asteroid Bennu, the spacecraft will maneuver toward Apophis once its sample return capsule has been delivered to Earth [13].

This work aims to identify a possible bounded trajectory for one of RAMSES CubeSats, named Farinella, to study Apophis during the close encounter with the Earth, maximizing the scientific return and ensuring that the trajectory poses no risk of a collision with the asteroid.

1.2. Motivation

The dynamical environment around Apophis can be divided into two distinct regimes based on the distance from the Earth. Far from the encounter (both pre- and post-flyby), the dominant forces arise from Solar Radiation Pressure and the asteroid's gravity field. Consequently, strong candidates such as terminator orbits [12] or Resonant Terminator Orbit (RTO) [5] can be considered. Among the possible strategies, even hyperbolic arcs and hovering can be considered, accounting for an increased fuel consumption and complexity [2].

During the Earth Close Encounter (CE), expected on April 13^{th}, 2029, the strong gravitational pull of the Earth must be considered in addition to the other forces. This significant time-dependent perturbation can only be modelled by non-autonomous dynamical systems.

Traditional methods that rely on the computation of quasi-periodic orbits, such as the ones presented in [5], fail to detect bounded solutions in this environment due to the time-dependent perturbation caused by the Earth. This thesis aims to find bounded trajectories by applying the Lagrangian Descriptors (LD) method [27], which can qualitatively divide the phase space regardless of the time dependence or complexity of the dynamical environment, at the cost of propagating a high number of trajectories. This last downside is mitigated by considering a GPU-parallelized integrator.

1.3. Research question and objectives

The dynamical environment near Apophis is chaotic, especially considering the Earth's perturbative effect during the CE. This makes it difficult to identify regions of space where the trajectory will be bounded during this specific time frame. This work aims to answer the questions:

- *To what extent do Lagrangian Descriptors provide insight into the Apophis dynamical environment at the close approach with the Earth by revealing the structures that organize the phase space into regions of different behavior?*

The final objectives of this thesis are:

- *Find regions of bounded motion around Apophis during its close encounter with the*

Earth

- *Investigate the capability of different Lagrangian descriptors to reveal organizing structures in non-autonomous astrodynamics systems*
- *Assess the feasibility of bounded orbits in relation to Farinella navigation constraints*

1.4. Thesis Structure

The remainder of this work is organized as follows:

- **Chapter 1** provides an introduction to this work, defines the context, research question, and objectives of the thesis.
- **Chapter 2** presents a literature review covering the physical and dynamical characterization of Apophis, Farinella instruments and requirements, the augmented Hill problem, and the theory of chaos indicators.
- **Chapter 3** defines the dynamical environment at close approach, including the software implementation and GPU integrator.
- **Chapter 4** proposes a strategy to reduce the problem dimensionality.
- **Chapter 5** presents the results obtained using the proposed methodology.
- **Chapter 6** summarizes the conclusions of this work and presents insight to expand this thesis.

2 | Literature review

This chapter presents the state of the art relevant to this work. The first section includes the characterization of (99942) Apophis, detailing the orbital and physical properties and the expected dynamical effects of the 2029 Earth encounter. Within this context, the RAMSES mission is briefly presented, with a detailed discussion about Farinella instruments and navigation constraints. The review then moves to useful autonomous models near small bodies. Finally, a survey of Chaos indicators is presented, highlighting the strengths and weaknesses of each considered method.

2.1. (99942) Apophis

(99942) Apophis is a near Earth asteroid that caused concern when initially discovered since it presented a probability up to 2.7 % to impact the Earth in 2029. Subsequent measurements ruled out the collision risk relative to the 2029 encounter. It is now certain that Apophis will pass extremely close to the Earth, with the closest passage at 38000 km, inside the geostationary ring [18].

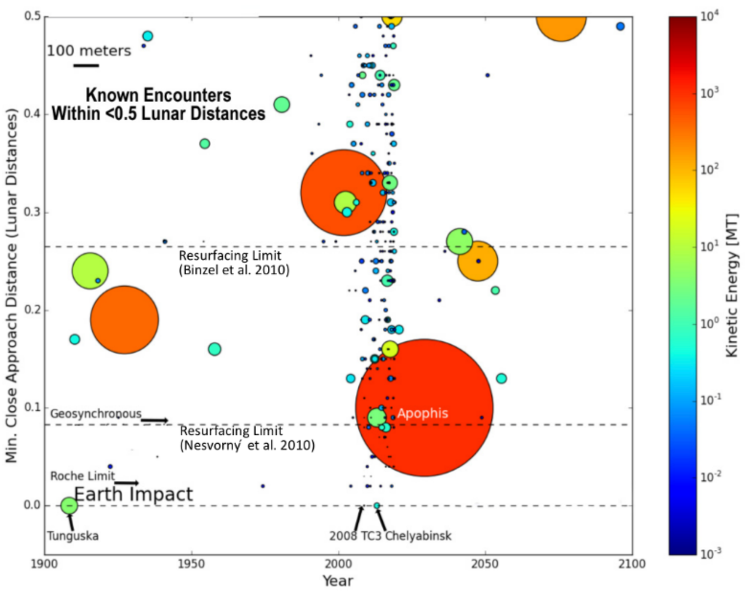

Figure 2.1: History of asteroids flyby with Earth, image from [4]

Apophis CE with the Earth in 2029 is characterized by a very low perigee and high kinetic energy, which constitutes a singular event when considering the history of asteroid flyby with the Earth since 1900, as highlighted in Figure 2.1 [4]. As mentioned in chapter 1, this is a valuable opportunity to study the internal structure of Apophis and providing valuable information to support planetary defense strategies. Notably, Apophis CE is close to the expected threshold for tidally induced seismicity, this can be an exceptional opportunity to study and constrain the asteroid interior.

2.1.1. Orbital and physical characterization

The most recent estimation of Apophis trajector is available in the Horizon system [22]. The CE is determined to be at 13 April 2029 21:45:03 UTC (in this work referred as t_{CE}); this value is obtained from the aforementioned data and the SPICE toolkit [1]. Figure 2.2a illustrates Apophis orbit in the heliocentric reference frame over the time interval $t_{CE} \pm 1.5$ years, while Figure 2.2b visualizes the fly-by in the time window $t_{CE} \pm 1$ days.

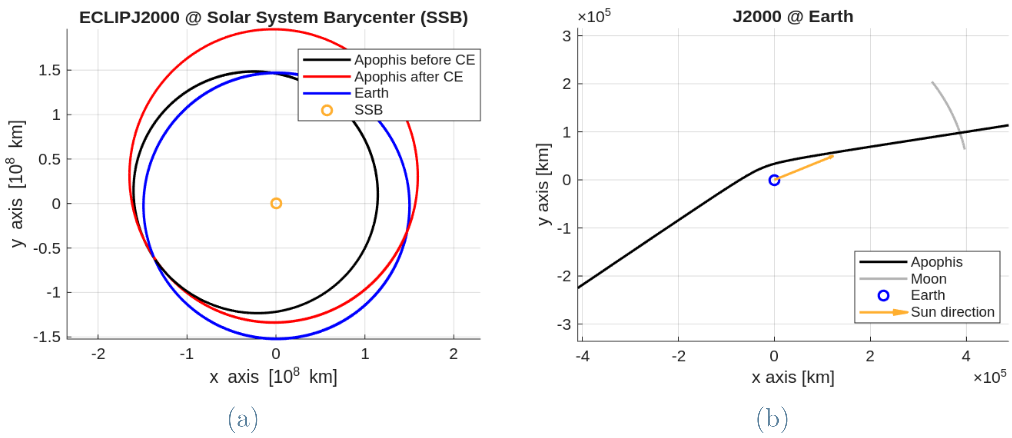

Figure 2.2: (a) Heliocentric orbit and (b) geocentric fly-by of Apophis.

The dynamical environment near Apophis is characterized by significant uncertainties that directly influence the trajectory design process. The current best estimate for the asteroid spin state come from [30], which classifies the asteroid as a Non-Principal Axis (NPA) rotor, specifically a Short-Axis Mode (SAM). An illustration of Apophis rotation is presented in Figure 2.3, while numerical parameters are reported in Table 2.1. Apophis is characterized by a 263 hours rotation period about its major axis and a 27.38 hour precession period of the long axis, resulting in an overall rotation period of 30.56 hours.

Apophis shape is elongated and possibly bifurcated. The current shape model, illustrated in Figure 2.4 [7], is a 3996 faces polyhedral shape that accounts for possible concavities.

Current estimates of Apophis bulk density, and therefore mass, are not precise and present a wide range of uncertainties. Recent studies consider various mass values to account for this uncertainty [6, 38].

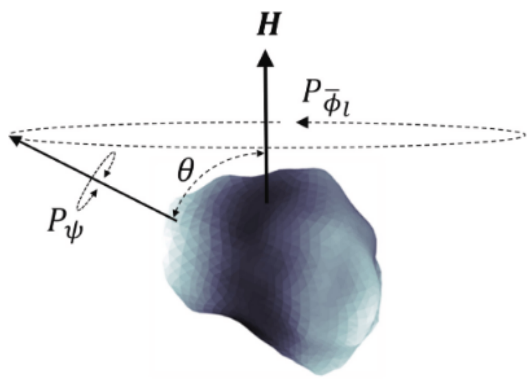

Figure 2.3: Visualization of Apophis spin state, image from [3]. θ represents the tilt angle, while the other parameters are detailed in Table 2.1.

Parameter description	Symbol	Value
Total mass (3 models) [38]	M	$(2.64,\ 4.50,\ 7.16) \times 10^{10}$ kg
Precession period	$P_{\bar{\phi}_l}$	27.38 h
Rotation period	P_ψ	263 h
Ecliptic longitude and latitude of $\boldsymbol{H}$	(λ_H, β_H)	$(250°, -75°)$
Long axis inertia ratio	I_l/I_s	0.61
Middle axis inertia ratio	I_m/I_s	0.965

Table 2.1: Apophis spin state pre-encounter parameters [30].

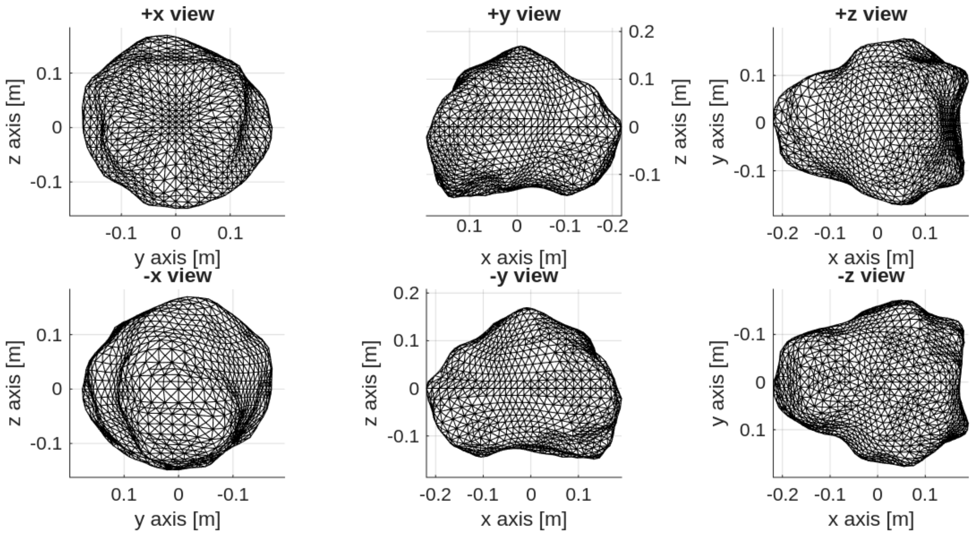

Figure 2.4: Apophis polyhedral shape in body reference frame [7].

2.1.2. Close approach effects

As previously mentioned, the Earth fly-by will have several consequences with varying degrees of certainty, summarized in Table 2.2 [2]. It is highlighted that the current uncertainty in the actual spin state is not negligible and causes several difficulties in predicting the spin state change. Current estimations show that after the fly-by, Apophis will likely stay in short-axis mode, with a small probability that the asteroid will enter long-axis mode. The likely scenario involves a 10° shift of the spin axis and a doubled or halved spin rate [3].

Physical effects	Confidence level
Spin state change	Certain
Shape and internal structure modifications	Unlikely
Seismic vibrations	Unlikely to possible
Surface alterations	Possible to likely

Table 2.2: Physical effects for Apophis 2029 encounter, from [2].

2.1.3. RAMSES missions and Farinella CubeSat

RAMSES is the candidate ESA mission to rendezvous with the asteroid (99942) Apophis before the Earth flyby [26]; the mission will build upon the heritage of the Hera mission [29], adapting the spacecraft design to meet the new requirements. RAMSES, like the Hera mission, will be constituted by a main spacecraft and two additional 6U-XL CubeSats to deploy near Apophis.

The CubeSats will support the main spacecraft with additional measurements to increase the scientific return. The tasks assigned to Farinella include the characterization of Apophis interior and surface properties. The CubeSat aims to accomplish these tasks with the use of an optical camera and a low-frequency radar: the optical camera is tasked with the acquisition of high-resolution images to map Apophis surface, while the low-frequency radar will perform measurements about Apophis interior structure, providing information on internal layers and density variations.

The CubeSat, in addition to the scientific optical camera and low-frequency radar, will carry an optical navigation camera to estimate the state by employing optical navigation algorithms, specifically center of brightness [31] and feature tracking methods [9]. To apply the center of brightness guidance method, Apophis must first be visible, and second, it should not saturate the field of view of the navigation camera. Based on preliminary studies of Farinella, the following two constraints must be accounted for:

- Radial distance to Apophis $r \in [1.4, 2.9]$ km, to ensure that Apophis does not occupy the entire field of view and obtain meaningful surface images [2];
- Phase angle $\phi < 100°$, the Farinella CubeSat must stay on the day side to ensure that Apophis is suitably illuminated.

2.2. Augmented Hill problem and periodic orbits

Navigation constraints, as well as payload requirements, impose limits on the spacecraft state, requiring a careful trajectory analysis to ensure spacecraft safety and high scientific return. Far from the CE, the dynamics of Farinella and any spacecraft in the vicinity of Apophis can be effectively described using the augmented Hill problem. This dynamical model is useful even in the CE window; since the Earth perturbation is significant only over a brief period of time, insights provided by the model valid outside of the CE window can aid in identifying regions where the trajectory is bounded. The Circular Restricted Three Body Problem (CRTBP) model is summarized to establish the general framework, then the characteristics of this model are progressively extended to the Hill problem considering Solar Radiation Pressure (SRP). This model is a particular case limit of the more general CRTBP, with the addition of the SRP perturbation considering the cannonball model.

2.2.1. Circular restricted three body problem

A full derivation of the model, as well as its characteristics, can be found in [11]. The CRTBP carries several assumptions with respect to the more general three-body problem. First of all, one of the three bodies is assumed to have an infinitesimal mass, and thus does not influence the motion of the other 2 (called primaries). Secondly, it is assumed that the primaries P_1 and P_2 move in circular orbits around their barycenter. The problem, then, is often expressed in the synodic reference frame, centered on the primaries barycenter and rotating with the same angular velocity as them. Specifically, the x-axis is aligned with the line connecting the primaries, the z-axis has the same direction as the angular velocity vector of the primaries, and the y-axis completes the right-handed frame. Figure 2.5 illustrate the reference frame. This introduction is necessary in order to go from a non-autonomous problem to an autonomous one; in fact, the equations of motion in the synodic frame do not depend explicitly on time.

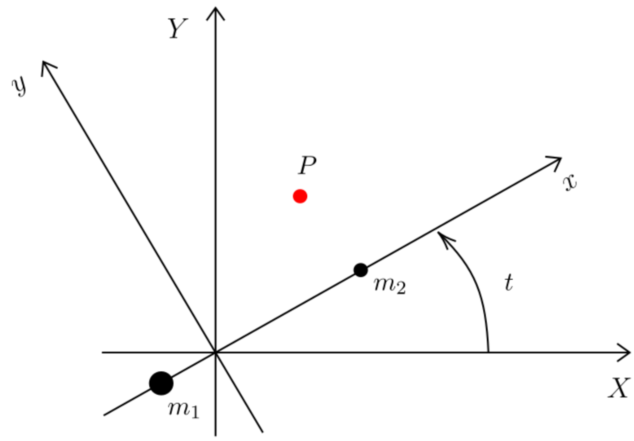

Figure 2.5: Representation of the synodic reference frame (x, y), where (X, Y) is an inertial reference frame. Image from [33].

Often, the problem is normalized selecting as unit of length the distance between the primaries, as unit of mass the sum of the primaries masses, and the unit of time is selected such that the period of the primaries orbit is equal to 2π. With this non-dimensionalization, the only free parameter of the model is the mass parameter defined as $\mu = m_2/(m_1 + m_2)$ where it is supposed that $m_2 < m_1$. The equations of motion of the infinitesimally small mass in this model, expressed in the synodic reference frame, are

$$\begin{cases} \ddot{x} - 2\dot{y} = U_x \\ \ddot{y} + 2\dot{x} = U_y \\ \ddot{z} = U_z \end{cases} \tag{2.1}$$

where

$$U(x, y, z) = \frac{x^2 + y^2}{2} + \frac{1-\mu}{r_1} + \frac{\mu}{r_2} \tag{2.2}$$

is the potential function. The subscript $U_{(\cdot)}$ denotes the derivative with respect to the specified variable. r_1 and r_2 represent the distance of the considered body to the primaries P_1 and P_2, given by

$$r_1 = \sqrt{(x+\mu)^2 + y^2 + z^2}, \text{ and } r_2 = \sqrt{(x-1+\mu)^2 + y^2 + z^2}.$$

The model is characterized by a constant of motion, the Jacobi constant, defined as

$$J = 2U(x, y, z) - (\dot{x}^2 + \dot{y}^2 + \dot{z}^2). \tag{2.3}$$

where U refers to Equation 2.2 for the CRTBP. This constant of motion is particularly useful; in fact, given any initial state, it is possible to determine regions of space in which the body can travel or not by using the constant of motion. The problem also presents 5 equilibrium points, called Lagrangian points, visualized in Figure 2.6.

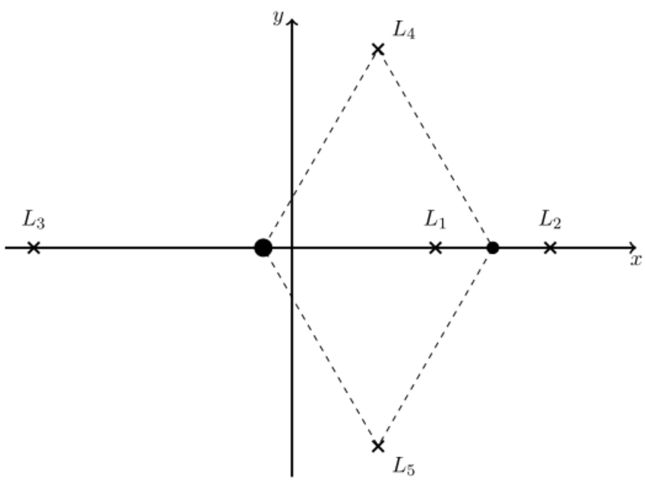

Figure 2.6: Visualization of the CRTBP equilibrium points, image from [21].

2.2.2. Hill problem

The Hill problem is a simplification of the CRTBP, it represents the limit case where μ approaches zero, focusing on the immediate vicinity of the smaller primary, also known as secondary. In mathematical terms, Hill's transformation consist in a translation of the reference system to the secondary body and a rescaling based on the mass parameter [36]

$$
\begin{aligned}
x &= X\mu^{1/3} + \mu - 1, \\
y &= Y\mu^{1/3}, \\
z &= Z\mu^{1/3},
\end{aligned}
\tag{2.4}
$$

where (X, Y, Z) represent coordinates in the Hill reference frame and (x, y, z) represent the coordinates in the synodic reference frame.

For clarity, (x, y, z) will refer to the Hill reference frame coordinates for the remainder of this section. Substituting Equation 2.4 into Equation 2.2, expanding the result in powers of $\mu^{1/3}$, and applying the limit $\mu \to 0$ yields the potential energy for the Hill problem

$$
U_{Hill} = \frac{3}{2}x^2 - \frac{1}{2}z^2 + \frac{1}{r}. \tag{2.5}
$$

Substituting this potential in Equation 2.1, yields the equations of motion for the Hill problem [21]

$$
\begin{cases}
\ddot{x} - 2\dot{y} = -\dfrac{x}{r^3} + 3x, \\[2ex]
\ddot{y} + 2\dot{x} = -\dfrac{y}{r^3}, \\[2ex]
\qquad\ \ddot{z} = -\dfrac{z}{r^3} - z.
\end{cases}
$$

Out of the five Lagrangian points in the CRTBP, only L_1 and L_2 survive. Since there is no free parameter in this model, they are fixed in space and occupy the position

$$
x = \pm\left(\frac{1}{3}\right)^{1/3}, \quad y = 0, \quad z = 0.
$$

A constant of motion can be found in the Hill problem, with the same form as in Equation 2.3 but considering the Hill potential. Since a constant of motion can be found, it is still possible to define forbidden regions of motion.

2.2.3. Augmented Hill problem

The Hill problem presented in the previous subsection can be expanded by considering several perturbations. The augmented Hill problem considers an additional term, the SRP. Assuming a spherical spacecraft, the equations of motion of this model are given by

$$\begin{cases} \ddot{x} - 2\dot{y} = -\dfrac{x}{r^3} + 3x + \beta, \\ \ddot{y} + 2\dot{x} = -\dfrac{y}{r^3}, \\ \ddot{z} = -\dfrac{z}{r^3} - z. \end{cases} \tag{2.6}$$

where β is the parameter that account for SRP. It is defined as [5]

$$\beta = \frac{G_1}{(m/A)\mu_{Sun}^{2/3}\mu_{cb}^{1/3}}$$

where G_1 is the Solar flux constant ($\approx 10^{14}$ kg km/s^2), μ_{Sun} and μ_{cb} are the gravitational parameter of the Sun and considered central body, and m/A is the mass to projected area of the spacecraft. Depending on the central body and considered spacecraft, it is possible to determine the free parameter of the model, Figure 2.7 shows different historical examples. In this case, the CubeSat Farinella will have a parameter near $\beta = 100$ ($\mu_{Aph} \approx 10^{-9}$ km^3/s^2, $m/A \approx 20$ kg/m^2).

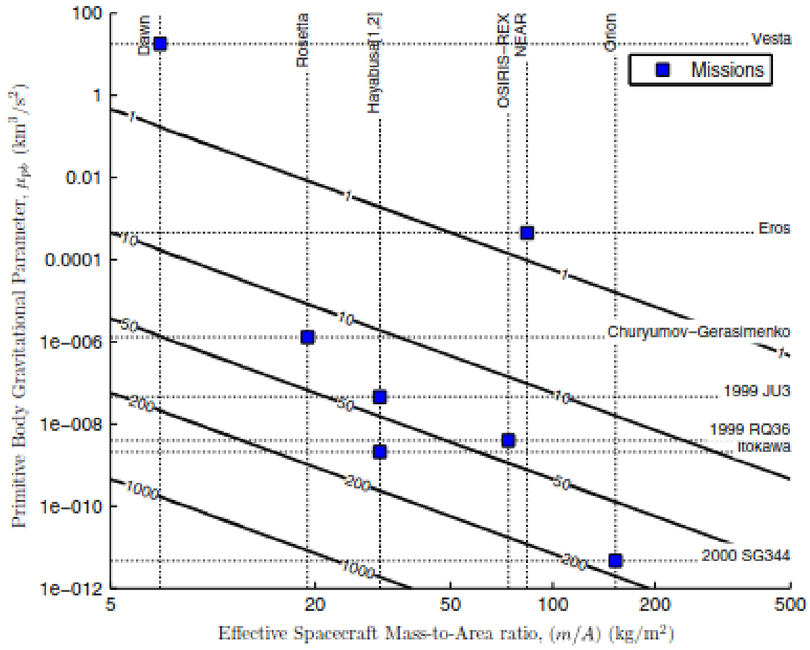

Figure 2.7: Countours of β as function of m/A and μ_{cb}, image from [5].

Even in this case, a potential can be defined as

$$U_{Hill,Aug} = \frac{3}{2}x^2 - \frac{1}{2}z^2 + \frac{1}{r} + \beta x.$$

such that it can be substituted into Equation 2.1 to obtain the equations of motion. The two equilibrium points from the Hill problem persist; however, their position now depends on β. Specifically, with increasing values of β, L_1 is shifted toward the Sun (-x direction in the Hill reference frame) and L_2 is shifted toward the central body.

It is noted that the model is still autonomous, and it is furthermore invariant under the following transformations [5, 21]

$$(y, t) \to (-y, -t),$$
$$(y, z, t) \to (-y, -z, -t),$$
$$(z) \to (-z).$$

Considering in particular the first one, if a given trajectory crosses the xz plane perpendicularly ($y = 0, v_x = 0, v_z = 0$) at two distinct time instants, then the given trajectory is a periodic orbit and symmetric with respect to the xz plane. Figure 2.8 illustrate this specific property.

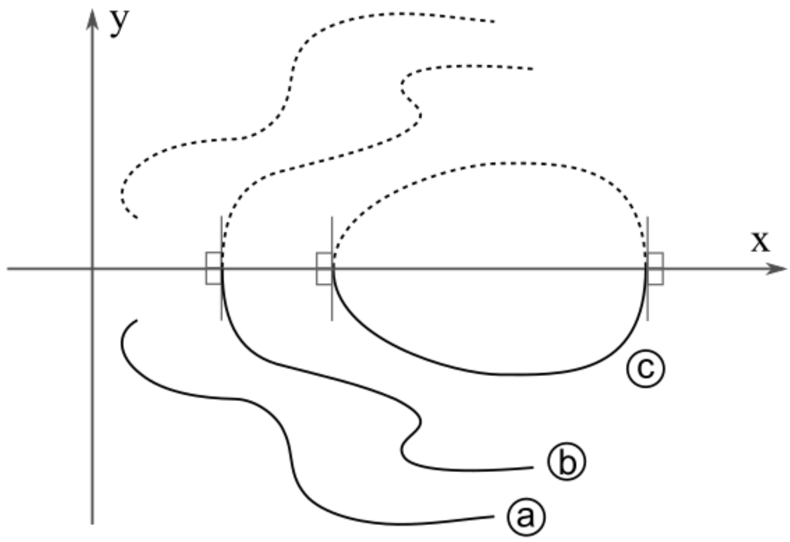

Figure 2.8: xz symmetry as periodicity condition, image from [21].

This allows to define a method to search for periodic orbits in the augmented Hill problem, as well as the Hill problem and CRTBP since the equations of motion remain invariant under this specific transformation. Given an initial state $(x_0, 0, z_0, 0, v_{y,0}, 0)$, in which the perpendicularity to the xz plane is enforced, differential corrections are used to find the values $(x_0, z_0, v_{y,0})$ for which the orbit has a second perpendicular crossing, and therefore is periodic [5, 21, 24, 25]. Other available methods to study the periodic orbits include the linearization at the equilibrium points and the study of the associated stable, unstable, and center manifolds [36]. Moreover, Poincaré maps and the study of the manifolds of periodic orbits can qualitatively separate trajectories belonging to different regions of the phase space, and even reveal connections between different periodic orbits [25, 32].

Among the periodic orbits of the augmented Hill problem, the relevant ones to this work are the terminator orbits [37] and RTO orbits [5, 6]. The RTO family bifurcates from specified resonances of the terminator family and shows promising characteristics for the Farinella CubeSat. These trajectories are formed by repetitive ellipses, as illustrated in Figure 2.9a. The image illustrates a Sun-side RTO, where the apocenter of each ellipse is on the Day side, leading to long periods of time in which Apophis is visible. Varying the energy and resonance number of the orbit allows to change the size of the orbit and the number of ellipses. Figure 2.9b, on the other hand, shows a dark-side RTO where the apocenters are on the night side, thus the spacecraft will experience long times on the night side and short times, with relatively high velocity, on the sun side.

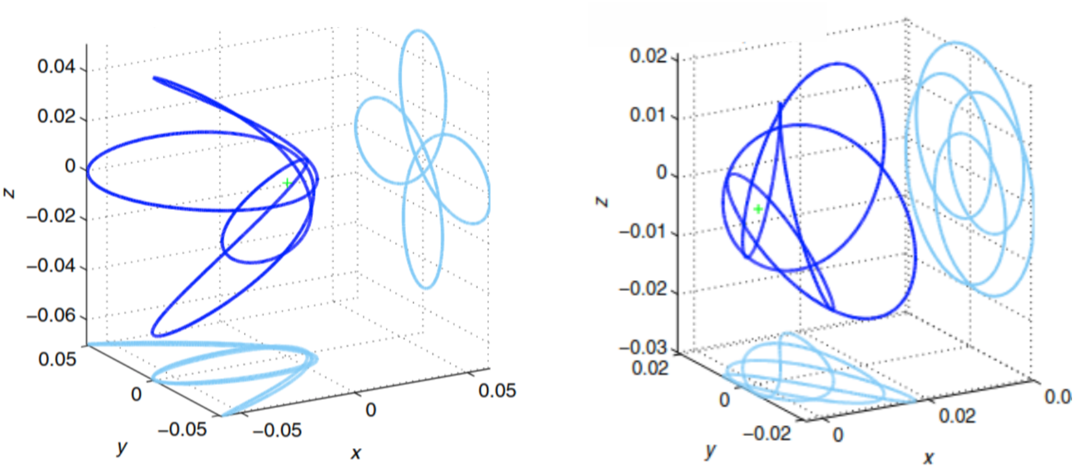

(a) Sun-side RTO. (b) Dark-side RTO.

Figure 2.9: RTO examples, images from [5]

While these orbits could work far from the flyby, the validity of this model breaks near the CE. The Earth's gravitational influence introduces a strong, time-dependent perturbation, necessitating the introduction of a non-autonomous model. In this regime, traditional periodic orbits do not survive, and the classical tools to study bounded motion cannot be applied.

2.3. Chaos indicators

In autonomous dynamical systems, like the models summarized in section 2.2, invariant manifolds of fixed points and periodic orbits can effectively separate the phase space in distinct regions characterized by different qualitative behaviour [25]. This allows to predict the qualitative behaviour of any given initial condition, avoiding the explicit integration. In non-autonomous systems or flows defined for a finite amount of time, however, these definitions are lost. In these cases, Lagrangian Coherent Structures (LCS) organizes the flow, and they can be seen as a generalization of invariant manifolds. A LCS is a specific material surface of the flow characterized by the local maximum attraction, repulsion, or shear [23]. Attracting and repelling LCS are known as hyperbolic LCS, visualized in Figure 2.10.

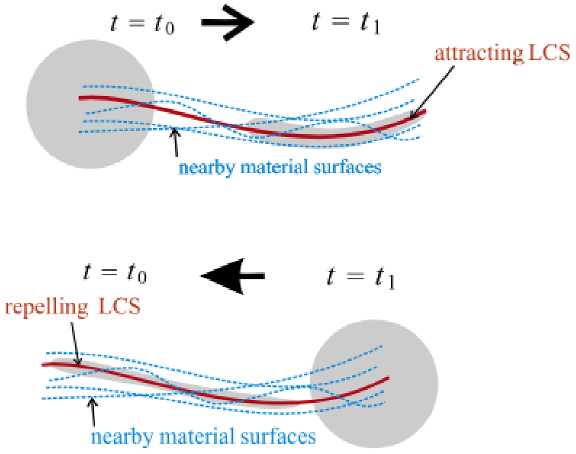

Figure 2.10: Attracting and repelling LCS, image from [23].

Originally, LCS were defined as ridges of the Finite Time Lyapunov Exponent (FTLE) field [35], however some counterexamples proved that this definition could cause false positives and negatives. A more rigorous formulation, known as variational theory, provides sufficient and necessary conditions to identify LCS, at the cost of being more computationally demanding [23]. More recently, a new heuristic technique has been introduced to detect phase space structures in general systems, known as LD [27].

2.3.1. Finite time Lyapunov exponents

Considering a dynamical system $\dot{\boldsymbol{x}} = f(\boldsymbol{x}, t)$, the flow map $\varphi_{t_0}^t(\boldsymbol{x}_0)$ describe the trajectory of the initial state $\boldsymbol{x}_0$, with the time t as independent variable. The State Transition Matrix (STM) of the dynamical system is defined as the gradient of the flow

$$\Phi(t; t_0, \boldsymbol{x}_0) = \nabla\varphi_{t_0}^t(\boldsymbol{x}_0) = \frac{\partial\varphi_{t_0}^t(\boldsymbol{x}_0)}{\partial\boldsymbol{x}_0}.$$

The STM is a mathematical tool to describe how small perturbations evolve in time, a key element to describe the geometry of LCS. The Euclidean norm of the separation between two arbitrary points at the time instant t can be defined as

$$||\delta\boldsymbol{x}(t)|| = \sqrt{\delta\boldsymbol{x}_0^T\Phi(t_0 + t; t_0, \boldsymbol{x}_0)^T \cdot \Phi(t_0 + t; t_0, \boldsymbol{x}_0)\delta\boldsymbol{x}_0}$$

The Cauchy-Green deformation tensor can be defined as

$$\boldsymbol{C}_{t_0}^{t_0+T}(\boldsymbol{x}_0) = \Phi(t_0 + T; t_0, \boldsymbol{x}_0)^T \cdot \Phi(t_0 + T; t_0, \boldsymbol{x}_0).$$

and maximum stretching occurs along the eigenvector of $\boldsymbol{C}_{t_0}^{t_0+T}(\boldsymbol{x}_0)$ associated with the maximum eigenvalue. The FTLE is defined as

$$\sigma_{t_0}^{T}(\boldsymbol{x}_0) = \frac{1}{|T|} \ln \sqrt{\lambda_{\max}(\boldsymbol{C}_{t_0}^{t_0+T}(\boldsymbol{x}_0))}$$

where $\lambda_{max}(\boldsymbol{A})$ is the maximum eigenvalue of $\boldsymbol{A}$. The LCS are then detected as ridges of the finite time Lyapunov exponent field, where the ridge can be a curvature ridge or a second derivative ridge [35]. The considered time T can be both positive and negative. For $T > 0$ repelling LCS are located, while for $T < 0$ attracting LCS are located.

This method is successfully applied to study trajectory behaviours in the planar elliptic restricted three-body problem [8, 19], even though it can be computationally expensive due to the computation of the Cauchy-Green deformation tensor. Regardless of these successful applications, counterexamples of LCS not detected by this method are provided; a more detailed method needs to be considered [23].

2.3.2. Variational theory

The variational theory approach, presented in [23], is introduced to develop a mathematically rigorous formulation and rule out false positives and false negatives detected by the FTLE method. This method aims at finding the material surface $M(t) \subset \mathbb{R}^n$ that maximizes the repulsion rate within the dynamical system $\dot{\boldsymbol{x}} = f(\boldsymbol{x}, t), f : \mathbb{R}^{n+1} \to \mathbb{R}^n$. At any point $\boldsymbol{x}_0$ belonging to the material surface, the geometry of the surface is defined by $\boldsymbol{t}_0 \in T_{\boldsymbol{x}_0} M(t_0)$ and $\boldsymbol{n}_0 \in N_{\boldsymbol{x}_0} M(t_0)$, the tangent and normal directions, belonging to the respective subspaces. It is noted, as underlined in Figure 2.11, that the tangential subspace is advected by the linearized flow but the normal subspace is not, that is $\Phi(t; t_0, \boldsymbol{x}_0)\boldsymbol{n}_0$ is not guaranteed to belong to $N_{\boldsymbol{x}_t} M(t)$.

In Figure 2.11, the linearized flow is represented as $\nabla F_{t_0}^{t}(\boldsymbol{x}_0)$, before indicated as the STM $\Phi(t; t_0, \boldsymbol{x}_0)$. The normal repulsion rate can now be expressed as

$$\rho_{t_0}^{t}(\boldsymbol{x}_0, \boldsymbol{n}_0) = \langle \boldsymbol{n}_t, \Phi(t; t_0, \boldsymbol{x}_0)\boldsymbol{n}_0 \rangle$$

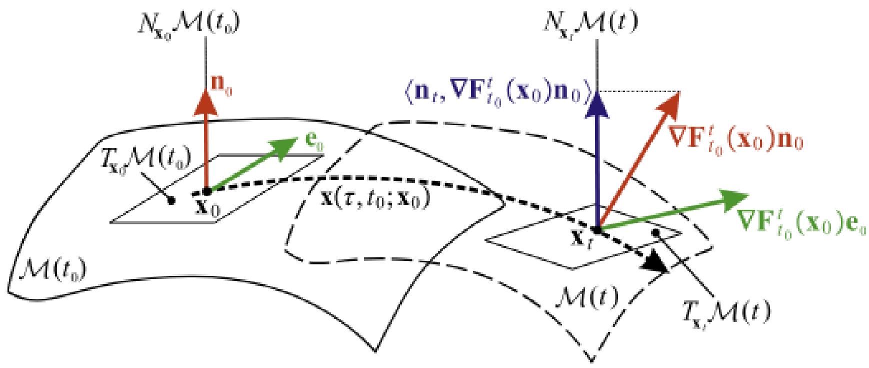

Figure 2.11: Geometry of material surface, tangential and normal subspaces, image from [23].

If $\rho_{t_0}^t(\boldsymbol{x}_0, \boldsymbol{n}_0) > 1$ for all $\boldsymbol{x}_0 \in M(t_0)$ and all $\boldsymbol{n}_0 \in N_{\boldsymbol{x}_0}M(t_0)$ then the surface is repelling. If instead $\rho_{t_0}^t(\boldsymbol{x}_0, \boldsymbol{n}_0) < 1$ $\forall \boldsymbol{x}_0, \boldsymbol{n}_0$ the surface is attracting. For the material surface to be a hyperbolic LCS, the repelling rate has to admit a local point-wise maximum, or minimum, among all neighboring material surfaces. Theorem 2.1 summarizes all sufficient and necessary conditions for a material surface to be a repelling LCS [16, 23].

Theorem 2.1. *Considering a compact material surface $M(t) \subset U$ over the time interval $[t_0, t_0 + T]$, $M(t)$ is a repelling LCS if and only if all the following conditions are satisfied for all $\boldsymbol{x}_0 \in M(t)$:*

1. $\lambda_{n-1}(\boldsymbol{x}_0, t_0, T) \neq \lambda_n(\boldsymbol{x}_0, t_0, T) > 1$;
2. $\boldsymbol{\xi}_n(\boldsymbol{x}_0, t_0, T) \perp T_{\boldsymbol{x}_0}M(t_0)$;
3. $\langle \nabla\lambda_n(\boldsymbol{x}_0, t_0, T), \boldsymbol{\xi}_n(\boldsymbol{x}_0, t_0, T) \rangle = 0$;
4. *The matrix $\boldsymbol{L}(\boldsymbol{x}_0, t_0, T)$ (Equation 2.7) is positive definite.*

$$
\boldsymbol{L} = \begin{pmatrix}
\nabla^2 \boldsymbol{C}^{-1}[\boldsymbol{\xi}_n, \boldsymbol{\xi}_n, \boldsymbol{\xi}_n, \boldsymbol{\xi}_n] & 2\dfrac{\lambda_n - \lambda_1}{\lambda_n \lambda_1}\langle \boldsymbol{\xi}_1, \nabla \boldsymbol{\xi}_n \boldsymbol{\xi}_n \rangle & \dots & 2\dfrac{\lambda_n - \lambda_{n-1}}{\lambda_{n-1}\lambda_1}\langle \boldsymbol{\xi}_{n-1}, \nabla \boldsymbol{\xi}_n \boldsymbol{\xi}_n \rangle \\
2\dfrac{\lambda_n - \lambda_1}{\lambda_n \lambda_1}\langle \boldsymbol{\xi}_1, \nabla \boldsymbol{\xi}_n \boldsymbol{\xi}_n \rangle & 2\dfrac{\lambda_n - \lambda_1}{\lambda_n \lambda_1} & \dots & 0 \\
\vdots & \vdots & \ddots & \vdots \\
2\dfrac{\lambda_n - \lambda_{n-1}}{\lambda_n \lambda_{n-1}}\langle \boldsymbol{\xi}_{n-1}, \nabla \boldsymbol{\xi}_n \boldsymbol{\xi}_n \rangle & 0 & \dots & 2\dfrac{\lambda_n - \lambda_{n-1}}{\lambda_{n-1}\lambda_n}
\end{pmatrix}
\tag{2.7}
$$

The first condition states that the largest eigenvalue of the Cauchy-Green deformation tensor is larger than one and has multiplicity one, ensuring that normal growth dominates the tangential growth. The second condition ensures that the eigenvector associated with the largest eigenvalue, $\boldsymbol{\xi}_n$, and thus the direction of maximum stretch, is perpendicular to the tangential space of $M(t)$. Both the second and third conditions ensure that the repulsion rate has a stationary point along the considered material surface. The last condition states that the repulsion rate admits a non-degenerate maximum along the normal direction of $M(t)$.

This approach is guaranteed to find LCS, at the cost of being computationally more demanding than the FTLE method. It is noted that in order to implement this method, Theorem 2.1 should be reformulated in order to ensure more robustness [17].

2.3.3. Lagrange descriptors

LD are introduced as a heuristic and easier method to detect underlying structures within a dynamical system [27]. The method consist in sampling a determined region in the phase space and propagating the states in both forward and backward time. The LD is then obtained as the integral of a positive quantity along a single trajectory, originally the Euclidean arc length of the trajectory itself [28]. Qualitatively similar trajectories will have similar LD values; on the other hand, if the trajectories behave differently, the LD value will differ. As a consequence, qualitative different regions will be separated by boundaries in the LD field [27].

Assuming a dynamical system $\dot{\boldsymbol{x}} = f(\boldsymbol{x}, t)$, a general initial state $\boldsymbol{x}_0$ and a finite time window $[t_0 - T,\ t_0 + T]$, the equation to compute the associated LD is

$$LD(\boldsymbol{x}_0, T) = \int_{t_0 - T}^{t_0 + T} f_{LD}(\varphi_{t_0}^{t}(\boldsymbol{x_0}))dt$$

where f_{LD} can be chosen as any positive value along the trajectory, the choices considered in this work are presented in Table 2.3. As remarked in [27], the choice of the integration time T is paramount to obtain meaningful results.

The LD method has shown good results in a wide range of fields. Historically, the first application is in the field of oceanic flows [28], and after this first success, the method spread to multiple fields, encompassing even orbital mechanics. In particular, the LD method is applied to find ballistic captures [32] and bounded trajectories in a binary asteroid system [33]. Since the nature of this method is heuristic, it presents the same possible downside of the FTLE, that is, the method is prone to false positives and negatives.

ID	Function
V_1	$\lvert v_x\rvert + \lvert v_y\rvert + \lvert v_z\rvert$
V_2	$\sqrt{v_x^2 + v_y^2 + v_z^2}$
A_1	$\lvert a_x\rvert + \lvert a_y\rvert + \lvert a_z\rvert$
A_2	$\sqrt{a_x^2 + a_y^2 + a_z^2}$
PQ	$\dfrac{1}{\kappa + 1}$ where $\kappa = \dfrac{\sqrt{(\boldsymbol{v} \cdot \boldsymbol{v})(\boldsymbol{a} \cdot \boldsymbol{a}) - (\boldsymbol{v} \cdot \boldsymbol{a})^2}}{(\boldsymbol{v} \cdot \boldsymbol{v})^{3/2}}$

Table 2.3: Different proposed positive quantities [32].

2.3.4. Comparison

Comparing all three presented methods to detect underlying structures that govern transport in a dynamical system, variational theory remains the most rigorous method since it encompasses necessary and sufficient conditions to find LCS, however it is also computationally demanding and the most complex method to implement. Both remaining methods can present false positives and negatives, the LD method is significantly simpler to implement since it requires only an integration along a trajectory. In contrast, the FTLE method requires the computation of the flow gradient. Consequently, the LD method is chosen to study the Apophis dynamical system at the CE with the Earth.

Finally, all methods considered in this section are particularly effective with planar phase spaces, however trajectory design problems inherently involve six dimensions. This dimensionality represents a challenge for analysis and visualization, therefore a dimensionality reduction strategy is developed and studied in this work to effectively study specific regions of the entire phase space.

3 | Dynamic model and numerical implementation

This chapter establishes the dynamical model in which the states are propagated, together with the assumptions and selected parameters. Afterward, an overview of the dynamical environment is proposed, and lastly, since numerous initial conditions need to be propagated, a GPU parallelization strategy is detailed. This parallelization significantly reduces the total computation time required to propagate large sets of initial conditions.

3.1. Equations of motion

The model will consider the non-spherical gravitational potential of Apophis, incorporated with spherical harmonics, as well as the third-body gravitational perturbations of Earth, Moon, and Sun. Additionally, solar radiation pressure is incorporated with a cannonball model, taking into account the parameters of the CubeSat.

The first order equations of motion are:

$$\begin{aligned} \dot{\boldsymbol{r}} &= \boldsymbol{v} \\ \dot{\boldsymbol{v}} &= \boldsymbol{a}_{SH} + \boldsymbol{a}_{SRP} + \boldsymbol{a}_{3b} \end{aligned} \tag{3.1}$$

where $\boldsymbol{r}$, $\boldsymbol{v}$ are the spacecraft position and velocity vectors in the inertial J2000 reference frame with the origin fixed at Apophis center. The models used for the central body gravitational effect and additional perturbations are presented below, while all model parameters referred to in the successive sections are presented in table 3.1. Sun, Earth, and Moon relative position with respect to Apophis, together with the relative gravitational parameters μ_i, are obtained from SPICE and the suggested kernels[1] [1].

[1]https://naif.jpl.nasa.gov/naif/toolkit.html (Last access at 18/02/2026)

Name	Value	Unit
Sun related constants		
Astronomical unit D_{AU}	$1.496\ 10^8$	km
Solar flux at 1 A.U. P_0	1367	W/m^2
Speed of light in the void c	$2.99792\ 10^5$	km/s
Universal gravitational constant G	$6.6743\ 10^{-20}$	$km^3/(kg\ s^2)$
Farinella parameters		
CubeSat mass m_{sc}	12.18	kg
CubeSat equivalent spherical area A_{sc}	0.5329	m^2
CubeSat area to mass ratio $B = A_{sc}/m_{sc}$	0.04375	m^2/kg
CubeSat reflectivity C_r	1.29	$-$
Apophis parameters		
Apophis mass M	$4.5\ 10^{10}$	kg
Apophis gravitational parameter $\mu_{Aph} = GM$	3.0034	m^3/s^2
Apophis volume (from polyhedron [7]) V_{Aph}	0.019826	km^3
Apophis density $\rho_{aph} = M/V_{Aph}$	2270	kg/m^3
Apophis reference radius R_{ref}	221.64	m

Table 3.1: Numerical parameters for equations of motion.

3.1.1. Perturbations

The cannonball model is used to model the solar radiation pressure. The model assumes the spacecraft geometry as a uniform sphere; thus, the perturbation is always directed along the sun direction. The equation to model the perturbation is

$$\boldsymbol{a}_{SRP} = \frac{P_0 D_{AU}^2 C_r B}{c} \frac{\boldsymbol{r} - \boldsymbol{r}_S}{||\boldsymbol{r} - \boldsymbol{r}_S||^3} \tag{3.2}$$

where $\boldsymbol{r}_s$ is the position vector of the Sun in the selected reference frame and given time instant. The SRP perturbation is considered only when the Spacecraft is free of eclipses, for the purpose of establishing this condition, Apophis is considered as a sphere of radius R_{ref}.

The third body perturbations can be obtained as

$$\boldsymbol{a}_{3b} = \sum_{i \in P} (\mu_i + \mu_{Aph}) \frac{\boldsymbol{r}_i}{||\boldsymbol{r}_i||^3} - \mu_i \frac{\boldsymbol{r} - \boldsymbol{r}_i}{||\boldsymbol{r} - \boldsymbol{r}_i||^3}.$$

It is noted that $\mu_{Aph} << \mu_i$ since major Solar System bodies have a mass significantly higher than Apophis, thus the perturbation can be rewritten as

$$\boldsymbol{a}_{3b} = \sum_{i \in P} \mu_i \left(\frac{\boldsymbol{r}_i}{||\boldsymbol{r}_i||^3} - \frac{\boldsymbol{r} - \boldsymbol{r}_i}{||\boldsymbol{r} - \boldsymbol{r}_i||^3} \right) \tag{3.3}$$

where P is the set of considered perturbing bodies, in this work the Sun, the Earth, and the Moon; μ_i is their relative gravitational constant and $\boldsymbol{r}_i$ their position vector with respect to Apophis.

3.1.2. Apophis gravitational acceleration

As illustrated in Figure 2.4, Apophis shape is highly irregular, thus corrections with respect to the spherical gravitational potential must be introduced. A high-detailed polyhedral model of Apophis is available, and trajectory design studies for OSIRIS-APEX [6] model the gravitational field with the polyhedron method [39, 41], considered the high fidelity model for an asteroid's highly irregular gravitational field. Spherical harmonics [10], on the other hand, are less precise, especially near the surface of the asteroid, and the convergence of the method is not guaranteed for extremely low altitudes; however, the method has a lower computational cost, in particular when truncated at low degree. This characteristic is paramount for this work, due to the high number of trajectories to consider. The following sections summarize the spherical harmonic mathematical model, a method to extract the spherical harmonic constants from a polyhedral model, and a comparison with the high-fidelity polyhedral model. The high fidelity model is summarized in Appendix A.

Apophis spin state

Regardless of the selected method to model Apophis gravity field, polyhedral or spherical harmonics, the spacecraft position vector needs to be rotated in the body-fixed reference frame. Afterward, the acceleration needs to be rotated back in the selected inertial frame to propagate the satellite state, in this case the Apophis-centered J2000 reference frame.

The close approach, as discussed in subsection 2.1.2, will induce a change in the spin state. Due to the current uncertainties in the spin state estimations, the change in both spin axis and spin rate is not clearly defined. Due to these reasons, for the scope of the trajectory analysis in this study, it is assumed that the Earth does not influence Apophis spin state during the flyby, an assumption consistent with other studies on trajectories near Apophis during the Earth CE [34]. The attitude presented in Figure 3.1 refers to the mean values of the pre-flyby estimation [30].

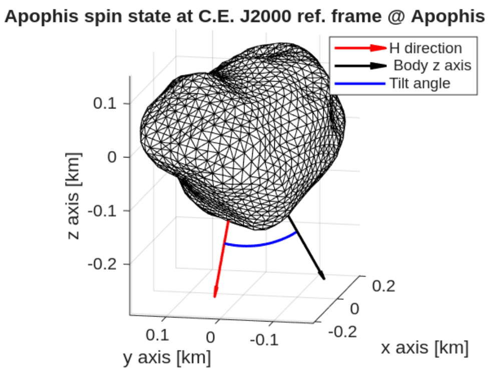

Figure 3.1: Apophis estimated attitude at Earth's CE.

Spherical harmonics model

The gravitational potential of a general body can be written as a summation of different contributions

$$V = \mu \sum_{n=0}^{\infty} \sum_{m=0}^{n} \frac{R_{ref}^n}{r^{n+1}} P_n^m(\sin\phi)(C_{n,m}\cos m\lambda + S_{n,m}\sin m\lambda)$$

where R_{ref} is a reference radius (in this work it is considered as the radius of the sphere circumscribing Apophis polyhedral model), μ is the gravitational planetary constant, P_n^m are associated Legendre polynomials and $C_{n,m}$, $S_{n,m}$ are constants that depend on the body shape. Lastly, radius r, latitude ϕ, and longitude λ are the spherical coordinates of the considered field point in the body-fixed reference frame. It is underlined that the method does not converge if $r \leq R_{ref}$; moreover, when considering the gradient of the potential to obtain the gravitational acceleration in spherical coordinates, there is a singularity at the poles ($\phi = \pm\pi/2$). The Cunningham method [10], summarized below, avoids this singularity and provides a recursive method to compute the potential. The characteristic of this method to avoid any singular points external to the central body is advantageous in the context of this work. In fact, multiple initial conditions need to be propagated and the presence of polar singularities in the gravitational field could lead to numerical issues during the integration.

Following the Cunningham derivation, the gravitational potential is defined with complex numbers

$$
\begin{aligned}
V_{n,m} &= \frac{P_n^m(\sin\phi)(\cos m\lambda + i\ \sin m\lambda)}{r^{n+1}}, \\
V &= \mu\ \mathrm{Re}\left(\sum_{n=0}^{\infty}\sum_{m=0}^{n} R_{ref}^n (C_{n,m} - i\ S_{n,m}) V_{n,m}\right).
\end{aligned} \tag{3.4}
$$

The recurrent equations are obtained by substituting the spherical coordinates with Cartesian ones and developing the Legendre polynomial functions

$$
\begin{aligned}
V_{0,0} &= \frac{1}{r} \\
V_{n,n} &= (2n-1)\frac{x + i\ y}{r^2} V_{n-1,n-1} \\
V_{n,n-1} &= (2n-1)\frac{z}{r^2} V_{n-1,n-1} \\
V_{n,m} &= \frac{2n-1}{n-m}\frac{z}{r^2} V_{n-1,m} - \frac{n+m-1}{n-m}\frac{1}{r^2} V_{n-2,m}
\end{aligned} \tag{3.5}
$$

Now, given any field point (x, y, z) in Cartesian coordinates, $V_{n,m}$ coefficients can be computed up to the maximum required order plus one, $n_{max} + 1$. With the gravitational potential coefficients obtained, the gravitational acceleration can be computed by firstly defining the derivatives of the coefficients

$$
\begin{aligned}
\frac{\partial V_{n,m}}{\partial x} &= -\frac{V_{n+1,m+1}}{2} + (n-m+2)(n-m+1)\frac{V_{n+1,m-1}}{2} \text{ if } \ m > 0, \\
&\quad -\frac{V_{n+1,1}}{2} - \frac{V_{n+1,1}^*}{2} \text{ if } \ m = 0 \\
\frac{\partial V_{n,m}}{\partial y} &= \frac{i\ V_{n+1,m+1}}{2} + (n-m+2)(n-m+1)\frac{i\ V_{n+1,m-1}}{2} \text{ if } \ m > 0, \\
&\quad \frac{i\ V_{n+1,1}}{2} - \frac{i\ V_{n+1,1}^*}{2} \text{ if } \ m = 0 \\
\frac{\partial V_{n,m}}{\partial z} &= -(n-m+1) V_{n+1,m}
\end{aligned} \tag{3.6}
$$

and then obtaining the accelerations

$$\boldsymbol{a}_{SH}^{body} = \mu_{Aph} \ \mathrm{Re} \left(\sum_{n=0}^{n_{max}} \sum_{m=0}^{n} R_{ref}^{n} (C_{n,m} - i \ S_{n,m}) \nabla V_{n,m} \right) \tag{3.7}$$

Defining the matrix to transform a vector from the J2000 reference frame to the Apophis reference frame A_{J2000}^{body}, the acceleration in the inertial reference frame can be expressed as

$$\boldsymbol{a}_{SH} = (A_{J2000}^{body})^T \boldsymbol{a}_{SH}^{body}$$

where the acceleration in the body frame is obtained with Equation 3.7, and the relative functions $V_{n,m}$ are expressed considering the position of the spacecraft in the body-fixed reference frame.

Mathematically, the model diverges if the field point is situated inside the circumscribing sphere. Therefore, the condition $r \leq R_{ref}$ is used as a termination criterion: any trajectory that satisfies this condition is classified as a surface impact, and the numerical integration is stopped. While intersecting this sphere does not strictly guarantee a physical collision with Apophis, such trajectories would cross a region of space characterized by extremely low altitudes. Considering the uncertainties on the polyhedron shape and assumed mass, these trajectories are conservatively classified as surface impacts.

Spherical harmonics coefficients

With the Cunningham method outlined, the last step consists of obtaining the coefficients $C_{n,m}, \ S_{n,m}$. They are defined as mass integrals of the extended body, and a particular method can be applied if the considered central body model is a polyhedron [40].

The exact formulas for the spherical harmonics coefficients are

$$\begin{bmatrix} C_{n,m} \\ S_{n,m} \end{bmatrix} = \iiint_{body} \begin{bmatrix} c_{n,m} \\ s_{n,m} \end{bmatrix} dm,$$

$$\begin{bmatrix} c_{n,m} \\ s_{n,m} \end{bmatrix} = \frac{1}{M}(2 - \delta_{0,m}) \frac{(n-m)!}{(n+m)!} \left(\frac{r}{R_{ref}} \right)^n P_{n,m}(\sin \phi) \begin{bmatrix} \cos m\lambda \\ \sin m\lambda \end{bmatrix}.$$

Analogously to recurrent relations in the Cunningham method, it is possible to build the integrands $(c_{n,m}, \ s_{n,m})$ with recursive relations:

$$
\begin{aligned}
\begin{bmatrix} c_{0,0} \\ s_{0,0} \end{bmatrix} &= \frac{1}{M}\begin{bmatrix} 1 \\ 0 \end{bmatrix}, \qquad \begin{bmatrix} c_{1,1} \\ s_{1,1} \end{bmatrix} = \frac{1}{M}\begin{bmatrix} x/R_{ref} \\ y/R_{ref} \end{bmatrix} \\
\begin{bmatrix} c_{n,n} \\ s_{n,n} \end{bmatrix} &= \frac{1}{2n}\begin{bmatrix} x/R_{ref} & -y/R_{ref} \\ y/R_{ref} & x/R_{ref} \end{bmatrix}\begin{bmatrix} c_{n-1,n-1} \\ s_{n-1,n-1} \end{bmatrix} \\
\begin{bmatrix} c_{n,n-1} \\ s_{n,n-1} \end{bmatrix} &= \frac{z}{R_{ref}}\begin{bmatrix} c_{n-1,n-1} \\ s_{n-1,n-1} \end{bmatrix} \\
\begin{bmatrix} c_{n,m} \\ s_{n,m} \end{bmatrix} &= \frac{2n-1}{n+m}\frac{z}{R_{ref}}\begin{bmatrix} c_{n-1,m} \\ s_{n-1,m} \end{bmatrix} - \frac{n-m-1}{n+m}\left(\frac{r}{R_{ref}}\right)^2\begin{bmatrix} c_{n-2,m} \\ s_{n-2,m} \end{bmatrix}
\end{aligned} \tag{3.8}
$$

Often, the spherical harmonic coefficients, and therefore integrands ($c_{n,m},\ s_{n,m}$), are normalized to ensure that higher-order contributions stay in the same numerical range as the lower-order ones; this is often implemented to avoid numerical cancellation issues. It is underlined that in Equation 3.5 non-normalized coefficients are used, so particular care must be taken when computing and loading the coefficients. Indicating as $\bar{C}_{n,m},\ \bar{S}_{n,m}$ the normalized coefficients, the following relation can be used to go from one set to the other one (the relation is valid also for the integrand functions $c_{n,m},\ s_{n,m}$):

$$
\begin{aligned}
N_{n,m} &= \sqrt{\frac{(2-\delta_{0,m})(2n+1)(n-m)!}{(n+m)!}} \\
\begin{bmatrix} \bar{C}_{n,m} \\ \bar{S}_{n,m} \end{bmatrix} &= \frac{1}{N_{n,m}}\begin{bmatrix} C_{n,m} \\ S_{n,m} \end{bmatrix}
\end{aligned} \tag{3.9}
$$

Now, considering a triangular face of the polyhedron, a simplex can be defined with one vertex at the origin and the others at the 3 faces' vertices. The coordinate change $(x, y, z) \rightarrow (X_{Symp}, Y_{Symp}, Z_{Symp})$ can be considered:

$$
\begin{aligned}
x &= x_1 X_{Symp} + x_2 Y_{Symp} + x_3 Z_{Symp} \\
y &= y_1 X_{Symp} + y_2 Y_{Symp} + y_3 Z_{Symp} \\
z &= z_1 X_{Symp} + z_2 Y_{Symp} + z_3 Z_{Symp}
\end{aligned} \tag{3.10}
$$

where the simplex vertices are supposed to be at $(0, 0, 0)$, (x_1, y_1, z_1), (x_2, y_2, z_2), and (x_3, y_3, z_3). This transformation maps any simplex to the standard one, with vertices at (0,0,0), (1,0,0), (0,1,0), and (0,0,1). Applying this coordinate change, the integrands are now expressed in the form:

$$\begin{bmatrix} \bar{c}_{n,m}(X_{Symp}, Y_{Symp}, Z_{Symp}) \\ \bar{s}_{n,m}(X_{Symp}, Y_{Symp}, Z_{Symp}) \end{bmatrix} = \sum_{i+j+k=n} \begin{bmatrix} \bar{\alpha}_{i,j,k} \\ \bar{\beta}_{i,j,k} \end{bmatrix} X^i_{Symp} Y^j_{Symp} Z^k_{Symp},$$

where $\bar{\alpha}, \bar{\beta}$ depend on the position of the simplex vertices.

In this form, the integration can be performed considering each face of the model, and therefore each simplex, obtaining the following equation

$$\begin{bmatrix} \bar{C}_{n,m} \\ \bar{S}_{n,m} \end{bmatrix} = \rho_{Aph} \sum_{simplices} \frac{\det J}{(n+3)!} \sum_{i+j+k=n} i!\ j!\ k!\ \begin{bmatrix} \bar{\alpha}_{i,j,k} \\ \bar{\beta}_{i,j,k} \end{bmatrix}, \tag{3.11}$$

where J is the Jacobian of the transformation detailed in Equation 3.10.

Table 3.2 reports the obtained spherical harmonic coefficients up to degree 8, considering the polyhedral model obtained in [7].

Comparison

The Cunningham model now needs to be verified against the high-fidelity one, the Polyhedron model detailed in Appendix A. Different values of n_{max} are considered, Figure 3.2 illustrates the error in percentage for various degrees and orders. In this work, $n_{max} = 8$ is selected as the optimal trade-off between computational effort and model fidelity.

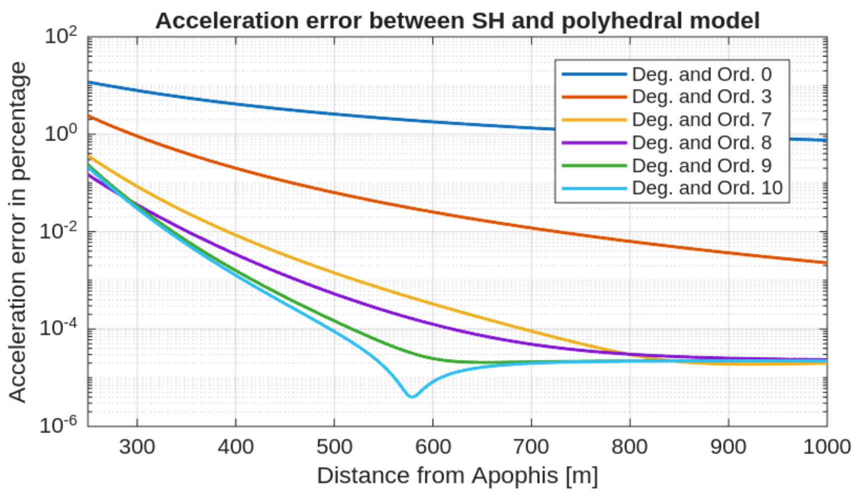

Figure 3.2: Error between spherical harmonics and polyhedron models in percentage.

Deg	Ord	C	S	Deg	Ord	C	S
0	0	1.000	0.000	6	2	-4.395 10^{-4}	-4.841 10^{-4}
1	0	-6.130 10^{-3}	0.000	6	3	-7.423 10^{-4}	-3.432 10^{-4}
1	1	1.345 10^{-2}	1.988 10^{-4}	6	4	3.299 10^{-4}	5.017 10^{-4}
2	0	-2.017 10^{-2}	0.000	6	5	6.568 10^{-4}	6.982 10^{-4}
2	1	-5.634 10^{-5}	-5.619 10^{-6}	6	6	-7.753 10^{-4}	-6.266 10^{-5}
2	2	2.366 10^{-2}	6.331 10^{-5}	7	0	4.282 10^{-5}	0.000
3	0	7.929 10^{-3}	0.000	7	1	-4.438 10^{-5}	-9.202 10^{-5}
3	1	1.496 10^{-3}	-9.262 10^{-4}	7	2	-4.930 10^{-6}	-8.973 10^{-5}
3	2	-1.156 10^{-2}	-4.063 10^{-3}	7	3	-1.541 10^{-5}	6.958 10^{-5}
3	3	-1.278 10^{-2}	5.560 10^{-4}	7	4	-2.466 10^{-4}	1.713 10^{-4}
4	0	2.954 10^{-4}	0.000	7	5	5.305 10^{-4}	-2.442 10^{-4}
4	1	-5.574 10^{-4}	-1.737 10^{-4}	7	6	3.855 10^{-4}	-4.147 10^{-4}
4	2	8.469 10^{-5}	4.299 10^{-4}	7	7	-7.204 10^{-4}	6.713 10^{-5}
4	3	4.284 10^{-4}	1.291 10^{-3}	8	0	3.699 10^{-5}	0.000
4	4	2.174 10^{-4}	5.134 10^{-4}	8	1	-1.314 10^{-4}	-9.286 10^{-5}
5	0	-1.001 10^{-3}	0.000	8	2	-1.731 10^{-4}	1.748 10^{-4}
5	1	-7.521 10^{-4}	-6.432 10^{-5}	8	3	2.289 10^{-4}	2.014 10^{-4}
5	2	1.379 10^{-3}	8.293 10^{-4}	8	4	2.102 10^{-4}	-2.842 10^{-4}
5	3	1.450 10^{-3}	1.049 10^{-4}	8	5	-2.506 10^{-4}	-2.931 10^{-4}
5	4	-8.578 10^{-4}	-7.555 10^{-4}	8	6	-4.780 10^{-5}	1.349 10^{-6}
5	5	-3.120 10^{-3}	4.366 10^{-4}	8	7	1.271 10^{-4}	1.552 10^{-4}
6	0	4.344 10^{-4}	0.000	8	8	-2.169 10^{-4}	-9.589 10^{-5}
6	1	2.897 10^{-4}	-5.255 10^{-6}				

Table 3.2: Normalized spherical harmonics coefficients up to degree and order 8 for Apophis gravity model.

3.1.3. Dynamical environment

In this section, the magnitude of the considered accelerations is analyzed. The third body perturbations are restricted to the Earth, the Moon, and the Sun. This specific choice is a trade-off between model fidelity and computational effort; in fact, a high-fidelity model requires all major solar system bodies. The three selected bodies represent the dominant perturbations within the considered time frame: the Earth and Moon are selected due to their proximity to Apophis near the CE, as seen in figure 2.2b, while the Sun is chosen due to its dominant mass.

Acceleration magnitudes are presented in Figure 3.3. Shaded intervals are used to represent temporal variations in Figure 3.3a and changes in distance in Figure 3.3b. It is highlighted that the acceleration due to Apophis gravitational field decreases rapidly as distance increases, while the third-body perturbations rise, especially the Earth perturbation at the CE. The solar radiation pressure remains constant since the asteroid-Sun distance barely changes in the considered time window. Figure 3.3b illustrates the temporal variations of the considered perturbations. It is noted that the Earth's influence can even surpass Apophis gravity in magnitude for some configurations and for a very brief period of time. The Moon's perturbation is similar in duration but does not reach values in the same order of magnitude as the Earth. As expected, solar radiation pressure and central body gravitational acceleration do not show temporal variations when considering a fixed point with respect to Apophis.

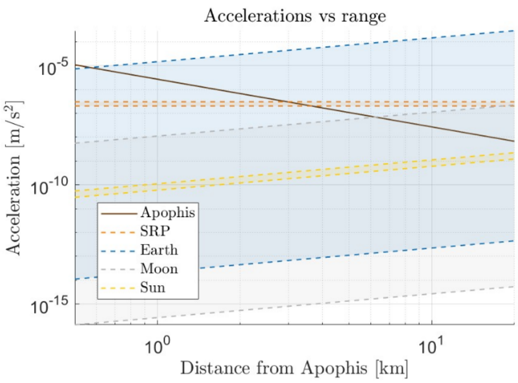

(a) Model accelerations with respect to Apophis distance.

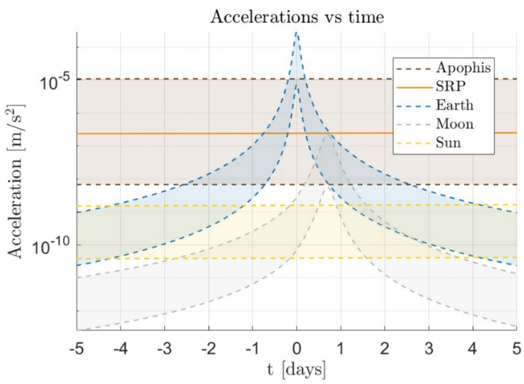

(b) Model accelerations with respect to time from CE.

Figure 3.3: Model accelerations magnitude, image from [2].

3.2. Software architecture and GPU acceleration

The LD approach, as well as all other approaches listed in section 2.3, require the definition of a region in phase space and the propagation of a high number of initial conditions. Propagating these states can be done in parallel, and while CPU parallelization is better for complex logic operations, GPU parallelization can handle a higher number of parallel processes, at the cost of slower double-precision calculations due to hardware limitations on low-grade components. In the context of LD computation and considering the model presented in section 3.1, GPU parallelization is more favorable, even considering low-grade hardware.

Below, a brief overview of GPU architecture and general architecture of the parallel integrator code implementation are presented.

3.2.1. GPU architecture

The GPU is inherently different from the CPU, and historically, it has been seen as a complementary device to the CPU with a massive number of cores that can carry out parallelized tasks. The relationship, architectures, and data exchange between CPU and GPU are summarized in Figure 3.4. It is worth highlighting the disparity of Arithmetic Logic Units (ALUs) between the 2 devices, and the possible bottleneck that is data transfer through the PCIe Bus.

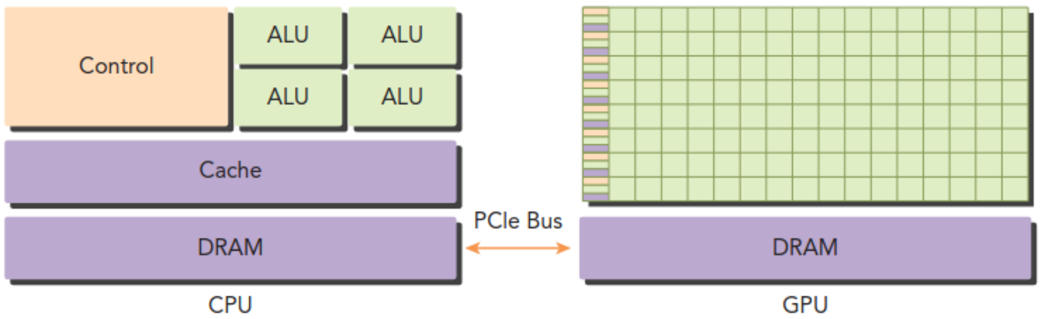

Figure 3.4: CPU-GPU relationship in CUDA program, image from [20].

CUDA, a general-purpose parallel computing platform and programming model, was introduced by NVIDIA in 2006 along with its own compiler *nvcc*, which separates the CPU host code from the GPU device code. The standard programming language used for the host and device code is C/C++ with suitable libraries. Memory management inside the GPU is paramount; in fact, it can be the main cause for a slow implementation. There are several memories available within the GPU [20], here only the ones used in the practical implementation are listed:

- Registers: fastest memory available, private to each thread, and the location of local variables. Spilled memory goes directly to a dedicated space inside the global memory; paying attention to register memory usage is paramount in order to avoid considerable slowdown.
- Constant memory: Extremely fast memory shared by threads, used for data that needs to be accessed multiple times between threads.
- Global memory: Largest and slowest memory in the GPU.

To exploit this different architecture, the software explores a parallelization strategy where the core software unit of the GPU, the kernel, is executed simultaneously by several threads. Specifically, at each thread is assigned a specific state to propagate. Consequently, all threads execute the same integrator step but for different assigned states, allowing to propagate multiple states at once.

3.2.2. Algorithm design

The CUDA program structure is presented in Figure 3.5, This software architecture adopts the parallelization strategy and design pattern originally proposed in [20].

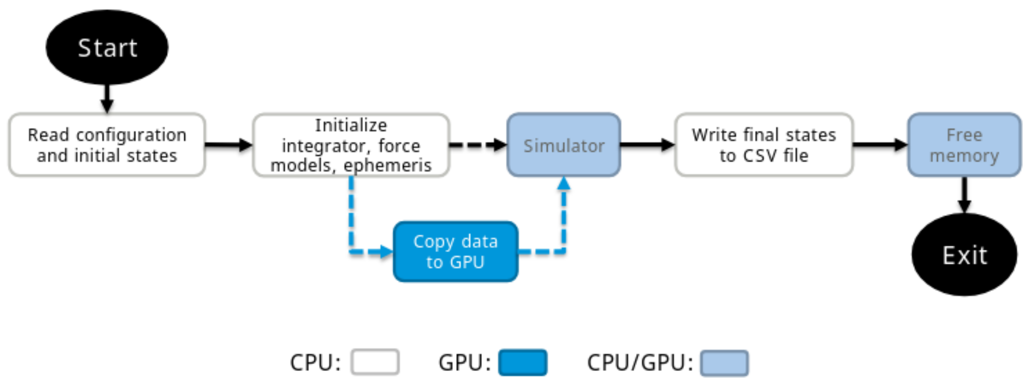

Figure 3.5: High-level software architecture, image from [20].

The CUDA software is concerned only with state propagation; initial state definitions, reference time, and other key parameters are set in a MATLAB program. Then MATLAB will launch the CUDA propagation and perform post-processing operations on the obtained LD field.

The relationship between the MATLAB script and GPU-accelerated integrator is highlighted in Figure 3.6. The file containing spherical harmonic coefficients and Apophis data is not generated by this MATLAB script due to the high computational effort required. For multiple runs, it is more efficient to compute the spherical harmonic coefficients once and save them permanently in a separate file. SPICE kernels are required in both MATLAB and the integrator software to track the precise state of celestial objects and ensure consistency between reference epochs.

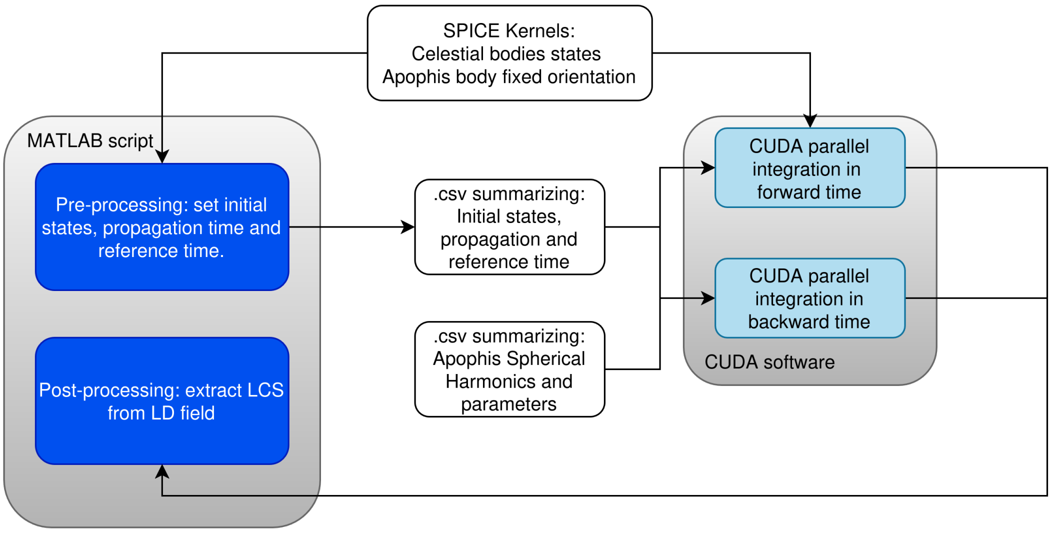

Figure 3.6: Data transfer architecture between MATLAB script and GPU-accelerated integrator.

Integrator choice

The selected numerical integrator is a variable-step Runge-Kutta 5^{th} order method, specifically the Dormand-Prince implementation [14]. The method consists of the following estimation for a given dynamical system $\boldsymbol{f}(t, \boldsymbol{x})$:

$$\begin{aligned}
\boldsymbol{x}_{n+1} &= \boldsymbol{x}_n + h_n \sum_{i=1}^{s} b_i \boldsymbol{k}_i \\
\hat{\boldsymbol{x}}_{n+1} &= \boldsymbol{x}_n + h_n \sum_{i=1}^{s} \hat{b}_i \boldsymbol{k}_i \\
\boldsymbol{k}_i &= \boldsymbol{f}\left(t_n + c_i h_n, \boldsymbol{x}_n + h_n \sum_{j=1}^{i-1} a_{ij} \boldsymbol{k}_j\right), \quad i = 1, \ldots, s
\end{aligned} \tag{3.12}$$

where h_n is the current time-step, $\boldsymbol{x}_n$ is the current state, $\boldsymbol{x}_{n+1}$, $\hat{\boldsymbol{x}}_{n+1}$ are the state estimates of the 5-th and 4-th order integrator, respectively. Coefficients b_i, $\hat{b}_i$, c_i, a_{ij} are defined in Table 3.3. The variable time-step is adjusted using Equation 3.13 [20], where $RelTol$ and $AbsTol$ are user-specified parameters; in this work, they are both set at 10^{-12}. Furthermore, in this implementation, only the position error is considered instead of the error of the entire state, and h_{n+1} is clipped in the range $[0.1, 2]h_n$ to avoid large changes. The step is rejected if $\epsilon > 1$; specifically, the time step is updated, and the integration step is repeated with the new value. It is underlined that the error is computed directly with the coefficients, and the 4th-order state is not computed directly. Moreover, the error considered in Equation 3.13 is the maximum one among all propagated trajectories since the time-step is shared by all parallel processes.

c_i	a_{ij}						b_i (5th)	$\hat{b}_i$ (4th)
0							$\frac{35}{384}$	$\frac{5179}{57600}$
$\frac{1}{5}$	$\frac{1}{5}$						0	0
$\frac{3}{10}$	$\frac{3}{40}$	$\frac{9}{40}$					$\frac{500}{1113}$	$\frac{7571}{16695}$
$\frac{4}{5}$	$\frac{44}{45}$	$-\frac{56}{15}$	$\frac{32}{9}$				$\frac{125}{192}$	$\frac{393}{640}$
$\frac{8}{9}$	$\frac{19372}{6561}$	$-\frac{25360}{2187}$	$\frac{64448}{6561}$	$-\frac{212}{729}$			$-\frac{2187}{6784}$	$-\frac{92097}{339200}$
1	$\frac{9017}{3168}$	$-\frac{355}{33}$	$\frac{46732}{5247}$	$\frac{49}{176}$	$-\frac{5103}{18656}$		$\frac{11}{84}$	$\frac{187}{2100}$
1	$\frac{35}{384}$	0	$\frac{500}{1113}$	$\frac{125}{192}$	$-\frac{2187}{6784}$	$\frac{11}{84}$	0	$\frac{1}{40}$

Table 3.3: Coefficients for the Dormand-Prince 5(4) method [14].

$$
\begin{aligned}
\epsilon &= \frac{||\boldsymbol{r}_{n+1} - \hat{\boldsymbol{r}}_{n+1}||}{AbsTol + ||\boldsymbol{r}_{n+1}||RelTol} \\
h_{n+1} &= h_n\ 0.9 \left(\frac{1}{\epsilon}\right)^{1/5}
\end{aligned}
\tag{3.13}
$$

A variable step integrator necessitates CPU-GPU communication at the end of every time step, and this can cause a considerable slowdown. Another possible issue with this integrator is its lack of precision, this is addressed once the results are obtained, comparing them with the MATLAB variable step 9^{th} order Runge-Kutta integrator.

Software structure

Algorithm 3.1 summarizes the GPU-accelerated integration process, where the kernel process involves the GPU threads working in parallel. The paragraphs below summarize some optimizations and crucial points of the GPU-accelerated integrator.

Algorithm 3.1 Parallel integrator

Set initial time $t = 0$ s, time step h according to time direction
Load initial states and model parameters on GPU
Load reference time t_{ref} on CPU
while abs(t) < abs(t_{ref}) **do**
    Load to GPU all required relative positions of Earth, Moon, and Sun
    Load to GPU all required Apophis body frame orientations
    (On GPU kernels) Perform integrator step
    (On GPU kernels) Retrieve maximum position error
    if Acceptable error (Equation 3.13) **then**
        Update integration time: $t = t + h$
        Update current states
    end if
    Update time step h
end while
Save current states to output file

The first optimization concerns the time-dependent parameters retrieved with the SPICE software, specifically the relative position of Earth, Moon and Sun, and the Apophis body-fixed reference frame orientation. To minimize communications between CPU and GPU, these parameters are retrieved and loaded in the GPU constant memory in batch for all intermediate Runge-Kutta stages.

Another numerical issue regards the evaluation of the spherical harmonic gravity model. Applying Equation 3.6 at once would require storing all potential terms in the register simultaneously, leading to register spilling and the consequent slowdown. Instead, a slide-window approach is considered, saving only the coefficients required to compute the acceleration at degree n, obtaining the acceleration terms corresponding to the considered degree, and then overwriting the unused coefficients in the next step. Moreover, the equations are rewritten using real numbers to further reduce the computational burden. With this approach, only the coefficients for 3 degrees need to be saved, instead of all of them.

One additional key issue is the termination condition for a surface impact. To account for this, each state is augmented with a collision flag. This flag is initialized at 1, and if a surface collision occur then the value is switched to 0. For all subsequent steps after a collision, the state is copied instead of propagated. This logic ensures that collided trajectories are not propagated and returns a flag to filter collision trajectories in the post-processing of the results.

Finally, with a massive number of propagated states, storing the full trajectory for all initial states will likely generate unmanageable file sizes. Since the computation of LD relies only on the accumulated scalar index, intermediate states are discarded during integration. Consequently, only the final state vector is saved and transferred back to the MATLAB script for the post-processing phase.

Lagrangian descriptors integration

To compute the LD indicator, the system state is augmented to include the scalar index. Defining the augmented state as $\boldsymbol{x}_{aug} = [\boldsymbol{x},\ \mathrm{LD}]$, Equation 3.14 describes both system dynamics and initial condition

$$\begin{cases} \dot{\boldsymbol{x}} = \boldsymbol{f}(t, \boldsymbol{x}) \\ \dot{\mathrm{LD}} = f_{LD}(\boldsymbol{x}) \end{cases}, \quad \boldsymbol{x}_{aug,0} = \begin{bmatrix} \boldsymbol{x}_0 \\ 0 \end{bmatrix} \tag{3.14}$$

where $\boldsymbol{f}(t, \boldsymbol{x})$ represents the equations of motion (defined in Equation 3.1) and $f_{LD}(\boldsymbol{x})$ is the positive scalar integrand function selected from the alternatives listed in Table 2.3.

To capture the full dynamical structure, the LD value is computed by summing the contributions from both forward and backward propagation over a finite time interval $t_{CE} \pm T$.

3.2.3. Performance evaluation

To evaluate the efficiency and scalability of the GPU-accelerated integrator software, several integrations with varying numbers of states are performed and timed. To ensure a consistent workload, the initial conditions are sampled from the same grid ($\alpha = 0, \theta = -50°$, the details on grid definition can be found in section 4.2). Moreover, to ensure that the evaluation is inherent to the considered enviroment and workload, initial conditions are propagated both in forward and backward time, considering a time window $t_{CE} \pm 14$ days. Figure 3.7 illustrates an approximately constant integration time until a delimited number of states is crossed. This result can have multiple causes, ranging from hardware capacity saturation to excessive CPU-GPU communication at each step due to the variable step integrator, or a combination of both. For this work, the result is considered acceptable, as a 200×200 discretized grid (40,000 states) provides a detailed LD field (section 5.2) to detect separate regions, and the integration time is manageable. As mentioned before, integration errors are quantified in section 5.2 once the results are presented.

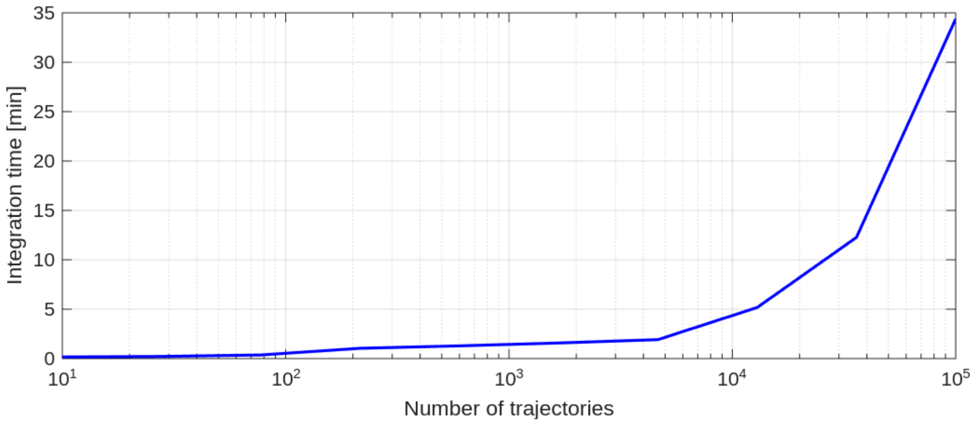

Figure 3.7: Scalability analysis of GPU-accelerated integrator.

4 | Methodology

In this chapter, the CE geometry is analyzed in detail, and a phase space dimensionality reduction from the full 6D to several planar 2D spaces is defined. Lastly, trajectory classifiers are introduced to better characterize different regions of the phase space.

4.1. Close encounter geometry

The CE geometry is peculiar; it can be noticed that the Earth's position is almost perpendicular to the Sun's direction, as depicted in Figure 4.1. In particular, if an osculating Hill refrence frame is defined as in Equation 4.1, considering the Sun-Apophis system at the CE epoch, it can be noticed that the Earth's direction is approximately along the y-axis of this reference frame.

$$
\begin{aligned}
\hat{\boldsymbol{x}} &= -\frac{\boldsymbol{r}_{sun}}{||\boldsymbol{r}_{sun}||} \\
\hat{\boldsymbol{z}} &= \frac{-\left(\boldsymbol{r}_{sun} \times \boldsymbol{v}_{Aph}\right)}{||\boldsymbol{r}_{sun} \times \boldsymbol{v}_{Aph}||} \\
\hat{\boldsymbol{y}} &= \hat{\boldsymbol{z}} \times \hat{\boldsymbol{x}}
\end{aligned}
\tag{4.1}
$$

From the underlying geometry, Earth's third body perturbation will be predominantly along the positive y-axis of the osculating Hill reference frame. According to the augmented Hill problem equations of motion symmetry, a necessary condition for an orbit to be periodic is to cross the xz plane perpendicularly ($y = 0,\ v_x = 0,\ v_z = 0$). It is hypothesized that trajectories crossing the xz plane perpendicularly at the CE possess the highest likelihood of remaining bounded far from the CE, since some configurations could assume periodic shapes characteristic of the augmented Hill problem even considering the Earth perturbing effect. This hypothesis gives a method to reduce the dimensionality of the problem, going from a 6-dimensional phase space to a 3-dimensional one. Given the heuristic nature of this assumption, the analysis extends to include small out of plane variations for the position vector.

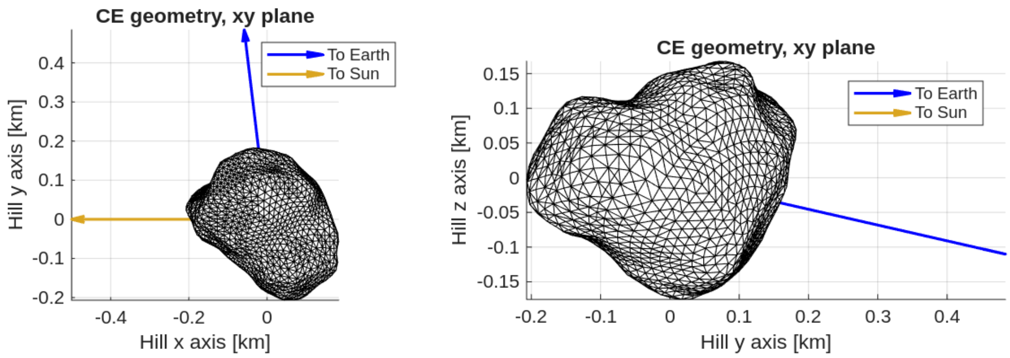

(a) CE geometry, xy plane.

(b) CE geometry, yz plane.

Figure 4.1: Close encounter geometry in osculating Hill reference frame, centered at Apophis.

4.2. Search strategy

Due to the heuristic argument presented earlier, the search is restricted to states that cross the xz plane perpendicularly at the moment of close approach. In the osculating Hill reference frame, these states are constrained to:

$$\boldsymbol{x}_0 = [x_0, 0, z_0, 0, v_{y,0}, 0]^T \tag{4.2}$$

Since the LD approach relies on visualizations of scalar fields, the analysis is most effective when applied to two-dimensional sections of the phase space. To achieve this, the position vector is parametrized using polar coordinates in the xz plane. The position is defined as

$$x_0 = r\cos\theta,\ \ z_0 = r\sin\theta.$$

With this setup, illustrated in Figure 4.2, a 2-dimensional grid can be formed varying the radial distance r and perpendicular velocity $v_{y,0}$, with fixed polar angle θ. Then the analysis can be iterated with different values of θ, in the interval $[-180°, 180°]$.

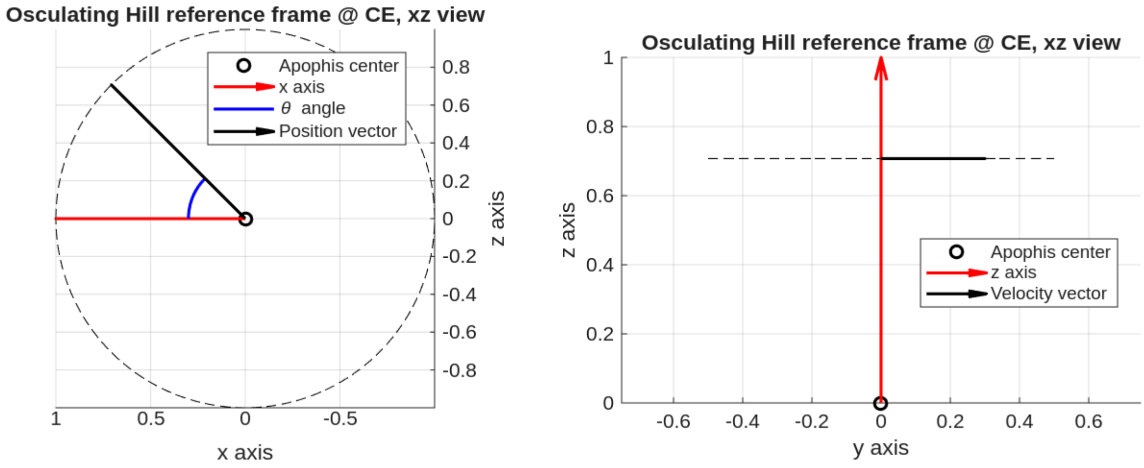

(a) xy plane. (b) yz plane.

Figure 4.2: Visualization of position vector parametrization.

To account for the slight misalignment of the Earth direction with the y-axis, an additional parametrization is considered, introducing the angle α that controls the xz out of plane component of the position vector. The state initial position in this modified parametrization is obtained as:

$$x_0 = r\cos\theta\cos\alpha, \; y_0 = r\sin\alpha, \; z_0 = r\sin\theta\cos\alpha.$$

A visualization of this parametrization is provided in Figure 4.3.

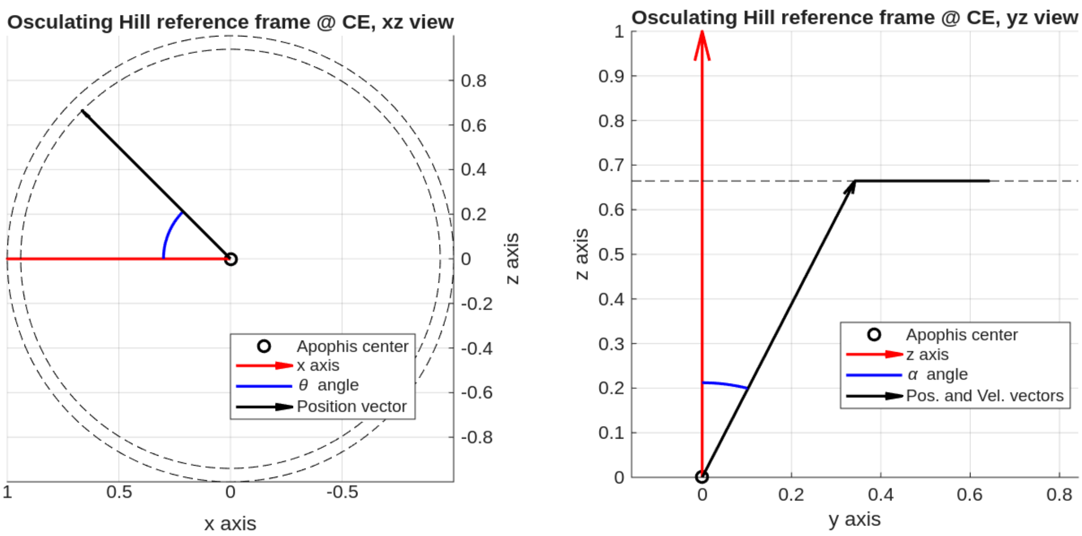

(a) xy plane. (b) yz plane.

Figure 4.3: Visualization of alternative position vector parametrization.

It is specified that the osculating Hill reference frame is used only in the definition of the initial states at the CE to exploit the particular geometry of the environment, the subsequent numerical integration is performed in the Apophis-centered J2000 inertial frame. The velocity component specified in Equation 4.2 is treated as an inertial velocity component expressed in the osculating frame orientation. To obtain the inertial J2000 initial state, a rotation matrix is applied to both position and velocity vectors at the epoch of close approach, omitting non-inertial terms due to the arbitrary values that will be considered in the search.

4.3. Trajectory classifiers definition

To verify the LD results and recognize the qualitative characteristics of different phase space regions, the entire set of considered initial conditions is divided into five different subsets. The definition of these subsets is reported in Table 4.1, where $\bar{r}$ is a parameter to identify escaped trajectories; in this work, $\bar{r} = 5$ km.

Subset	Definition
Crash set (K_T)	$\exists t \in [-T, T] : r(t) < R_{ref}$
Bounded set	$r(T) < \bar{r},\ r(-T) < \bar{r},\ \boldsymbol{x}_0 \notin K_T$
Bounded forward set	$r(T) < \bar{r},\ r(-T) \geq \bar{r},\ \boldsymbol{x}_0 \notin K_T$
Bounded backward set	$r(T) \geq \bar{r},\ r(-T) < \bar{r},\ \boldsymbol{x}_0 \notin K_T$
Escape set	$r(T) \geq \bar{r},\ r(-T) \geq \bar{r},\ \boldsymbol{x}_0 \notin K_T$

Table 4.1: Trajectory classifiers definition.

It is important to note that the classification of initial conditions, like the LD field, is inherently dependent on the propagation time. The selection of this parameter is discussed in section 5.1, where a trade-off analysis is performed to identify the best choice.

The classification process involves both numerical integration and post-processing. As detailed in section 3.2, the surface impact condition is evaluated at each step of the numerical integrator; if a trajectory impact Apophis circumscribing sphere ($r < R_{ref}$), the propagation is terminated for the specific trajectory. The escape condition is evaluated similarly, but it does not terminate the numerical integration of the trajectory. This ensures that the LD indicator remains consistent among escaped and bounded trajectories. To account for the different possibilities, the crash flag is modified to keep track of all three possibilities (surface impact, bounded, or escaped) with different logical values since these states are mutually exclusive. Finally, these status flags are computed for both forward and backward propagation, and the subsets defined in Table 4.1 are derived by combining the resulting pairs of flags to characterize the trajectory's global behaviour.

5 | Results

This chapter presents the results of this work, applying the model and methodology defined in previous chapters. The first section defines the considered time window and the LD function that will be applied to reveal the underlying dynamical structures. Then, selected regions of the phase space are investigated with the parametrizations detailed in section 4.2.

5.1. Lagrangian descriptor comparison

An accurate choice of integration time T and specific LD function is paramount to obtain meaningful results. To ensure these parameters are optimal, a preliminary analysis is performed.

This a priori investigation firstly scans the phase space to identify regions with bounded trajectories. The phase space region considered in section 4.2 is discretized with a resolution of 200×200 points, spanning the following intervals:

- Radial distance $r \in [400, 2500]$ m;
- Transverse velocity $v_{y,0} \in [-0.1, 0.1]$ m/s.

This grid is then propagated for varying polar angles θ. The angle is discretized in the interval $[-180°, 180°]$ with a step-size $\Delta\theta = 10°$. The out of plane angle is set to zero for this initial assessment ($\alpha = 0°$). With the initial conditions defined, each state is propagated forward and backward within the provisional time window $t_{CE} \pm 14$ days. For each planar region, the trajectories inside the bounded subset are counted; this metric serves as a method to identify polar angles where possible bounded motion can be found.

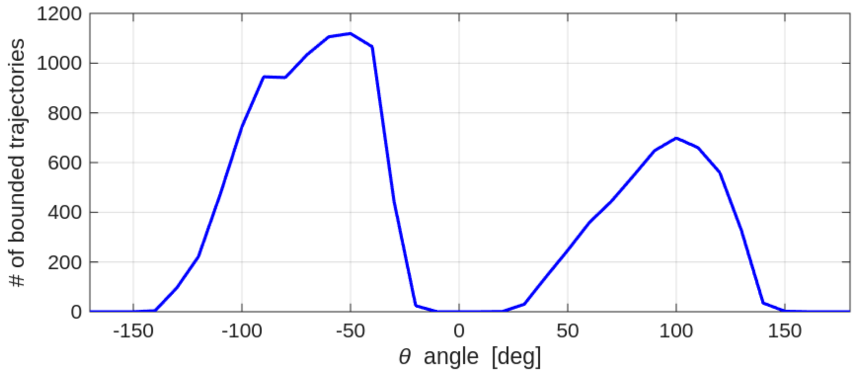

Figure 5.1: Number of bounded trajectories over different polar angles.

Two distinct peaks can be identified from Figure 5.1, identifying two values of polar angles where the number of bounded trajectories is at a local maximum. The value $\theta = -50°$ is arbitrarily selected to evaluate both the considered time window and the LD function. The latter is considered first, where all 5 choices presented in Table 2.3 are evaluated. Figure 5.2 illustrates both the trajectory classifiers of the selected planar phase space and the obtained LD fields for validation purposes. In the LD field, all crashed trajectories are not considered. From the images, PQ, V1, and V2 capture the subset divisions; ultimately, V1 is chosen since the regions are identified more easily from the relative LD field.

Once the LD function is fixed, the time window needs to be determined; three possibilities are considered: 10, 14, and 18 days from the Earth CE. Figure 5.3 illustrates the obtained results with different time windows. It is noted that for $T = 10$ days, the LD field is not able to detect all subset boundaries. Both $T = 14$ days and $T = 18$ days detect all the divisions among the defined subsets; $T = 18$ days present more clearly defined regions, so this time window is ultimately chosen. It is underlined that the definition of bounded trajectories (Table 4.1) changes with different selected time windows, therefore bounded trajectories are not guaranteed to retain this characteristic outside of the considered time window. This is evident in the studied figures, where the edges of the various subsets slightly move as different integration times are selected.

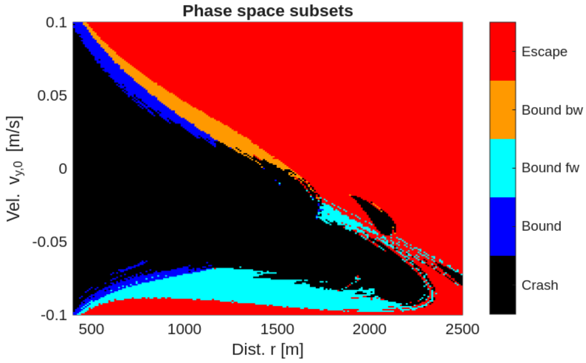

(a) Subsets of the selected phase space region.

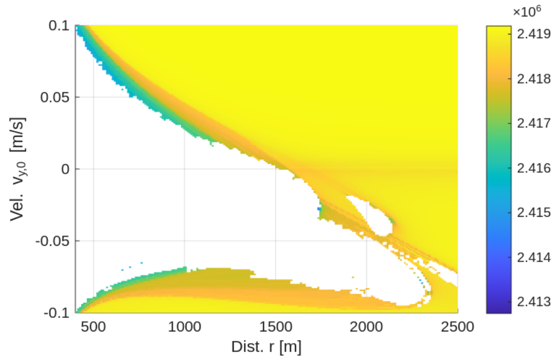

(b) PQ function.

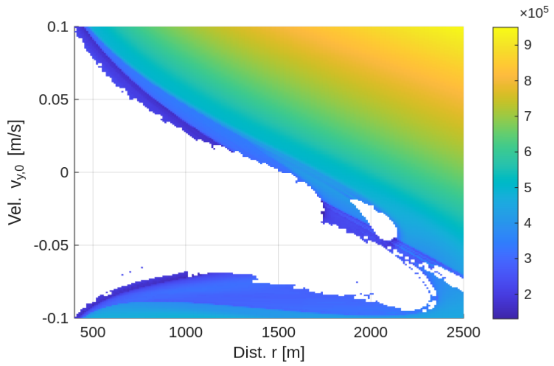

(c) V1 function.

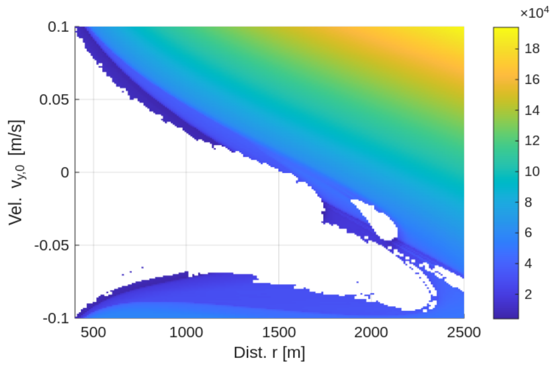

(d) V2 function.

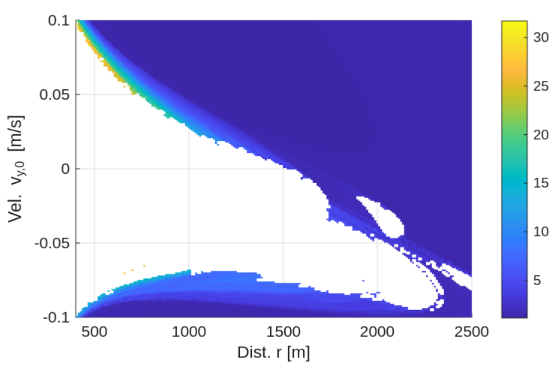

(e) A1 function.

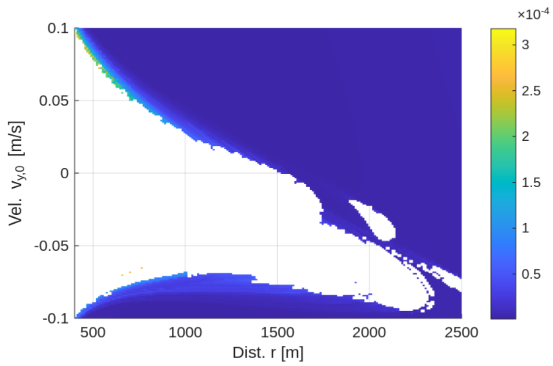

(f) A2 function.

Figure 5.2: Evaluation of LD functions, defined in Table 2.3.

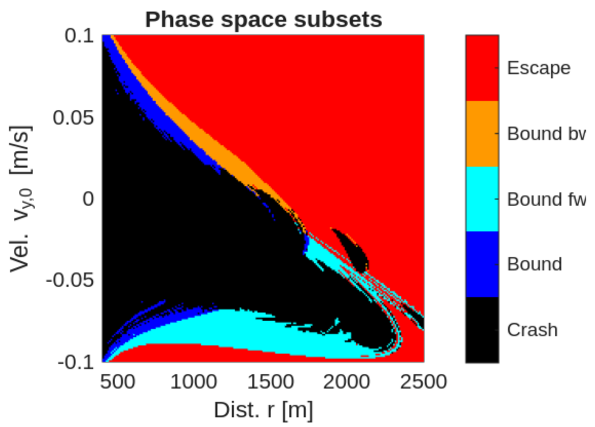

(a) Subsets of the selected phase space region, $T = 10$ days.

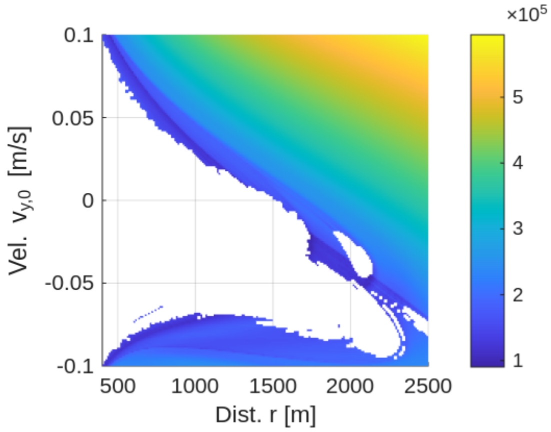

(b) Gradient magnitude, $T = 10$ days.

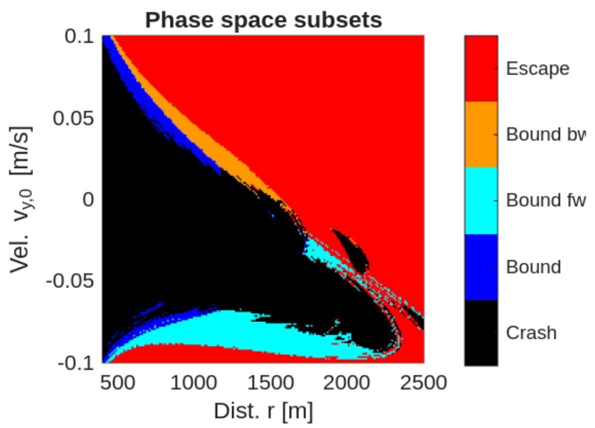

(c) Subsets of the selected phase space region, $T = 14$ days.

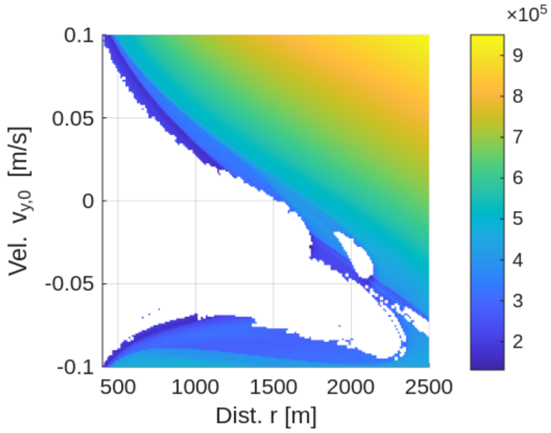

(d) Gradient magnitude, $T = 14$ days.

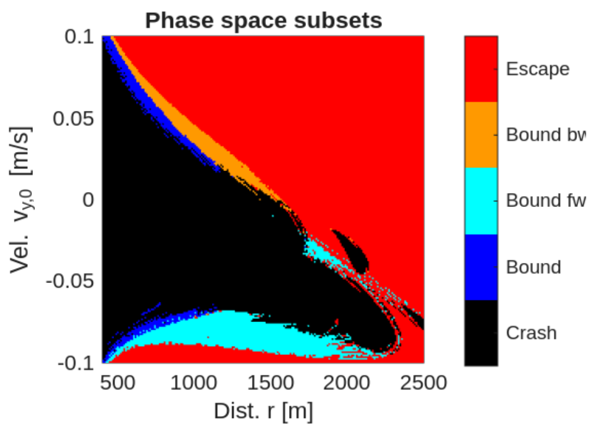

(e) Subsets of the selected phase space region, $T = 18$ days.

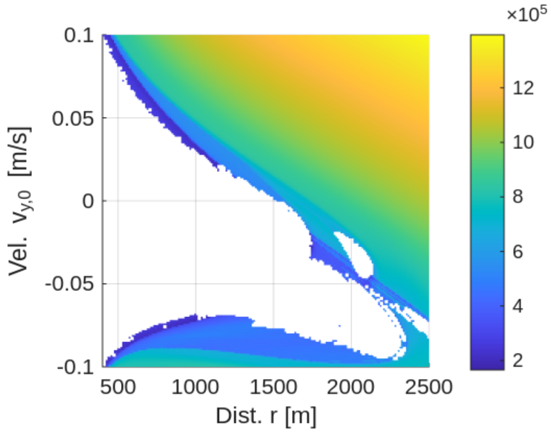

(f) Gradient magnitude, $T = 18$ days.

Figure 5.3: Evaluation of different integration time-windows.

5.2. Trajectory sampling

Now all detected regions of bounded motion are presented, together with some trajectories sampled from them. The θ interval is discretized in steps of $10°$, and the out of plane angle α is varied among three values: $-10°, 0°, 10°$. The selected grid for the radial position and transverse velocity is the same as the previous section. For each possible angle set the bounded trajectories are counted, results are reported in Figure 5.4. Numbers of bounded trajectories are computed considering a propagation time $T = 14$ days due to the high number of states and consequent computational effort, the LD maps will be computed using $T = 18$ days only for regions with bounded motion.

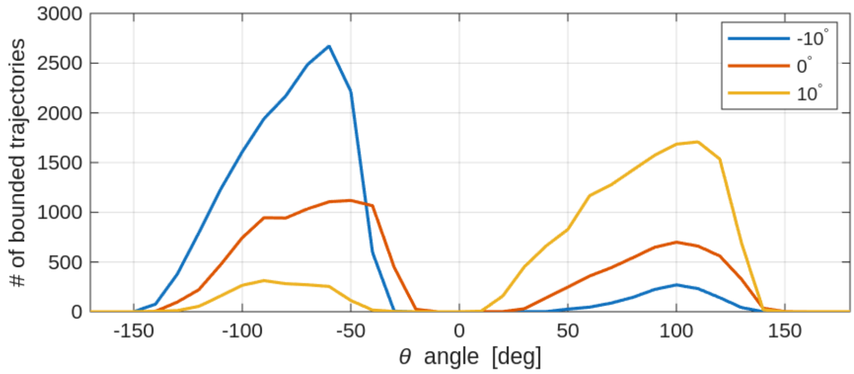

Figure 5.4: Number of bounded trajectories over different angle sets (α, θ).

From the results in Figure 5.4, 2 peaks are identified at $(\alpha = -10°, \theta = -60°)$, and $(\alpha = 10°, \theta = 110°)$. The sets $(\alpha = 0°, \theta = -50°)$ and $(\alpha = 0°, \theta = 100°)$ are also studied. All sampled trajectories in this chapter are obtained with the MATLAB variable step 9^{th} order Runge-Kutta numerical integrator, considering the same dynamical model as the one implemented in the GPU integrator. Both absolute and relative errors are set to 10^{-12}.

Figure 5.5 shows the regions defined by $(\alpha = 0°, \theta = 100°)$ and $(\alpha = 10°, \theta = 110°)$. It is possible to notice that the structures are similar, even if the latter presents a higher number of bounded trajectories and smaller neighbouring regions with partially bounded motion. The computed subsets and the LD field match correctly, some trajectories are sampled and visualized in Figure 5.6. The reported images show the range $r \in [400, 1400]$ m since all radial values in the range $[1400, 2500]$ m show either impacted or escape trajectories. As before, the LD field do not show the values for crashed trajectories.

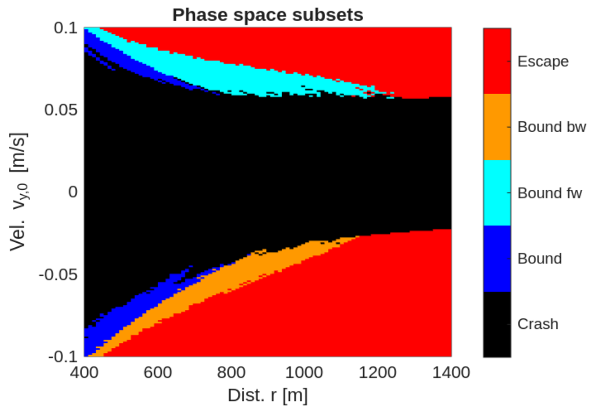

(a) $\alpha = 0°, \theta = 100°$ subsets

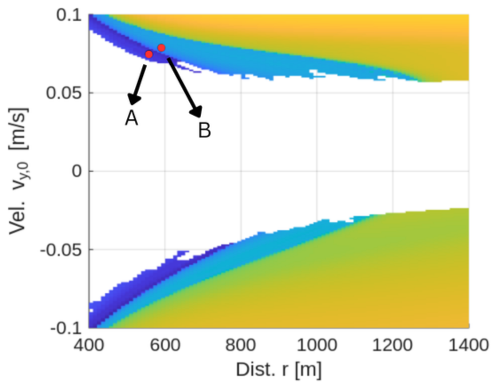

(b) LD field

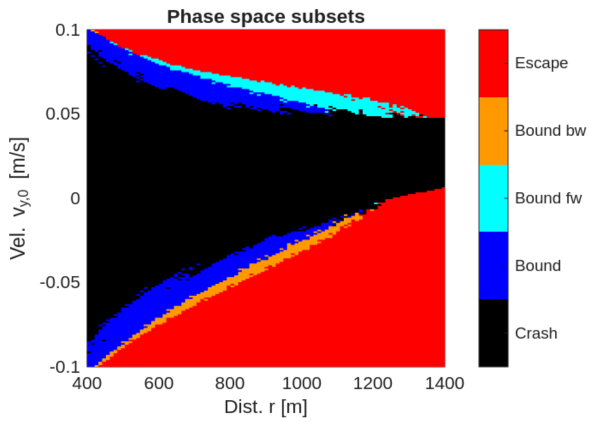

(c) $\alpha = 10°, \theta = 110°$ subsets

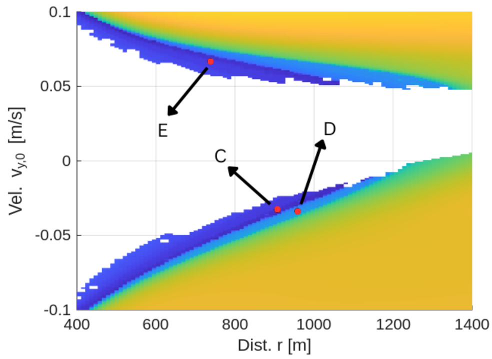

(d) LD field

Figure 5.5: $(\alpha = 0°, \theta = 100°)$ and $(\alpha = 10°, \theta = 110°)$ subsets and LD fields.

ID	x [m]	y [m]	z [m]	v_x [m/s]	v_y [m/s]	v_z [m/s]	Motion
A	74.7	-153	532	0.0302	-0.0646	-0.0228	Bounded
B	78.9	-162	562	0.0318	-0.0681	-0.0241	Bounded forward
C	321	-311	788	-0.0132	0.0282	0.0100	Bounded
D	340	-329	834	-0.0136	0.0290	0.0103	Bounded backward
E	262	-253	642	0.0269	-0.0577	-0.0204	Bounded

Table 5.1: Initial states, at Earth CE, of considered trajectories in Apophis centered J2000 reference frame for $(\alpha = 0°, \theta = 100°)$ and $(\alpha = 10°, \theta = 110°)$.

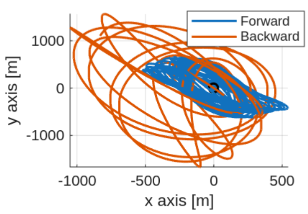

(a) A, xy plane

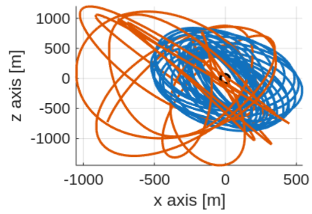

(b) A, xz plane

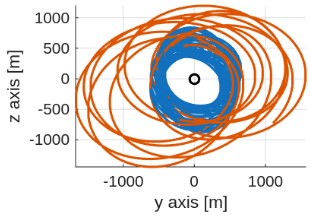

(c) A, yz plane

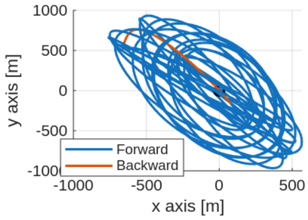

(d) B, xy plane

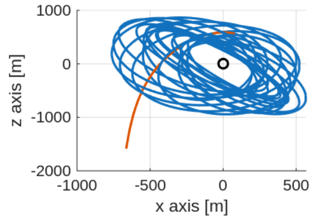

(e) B, xz plane

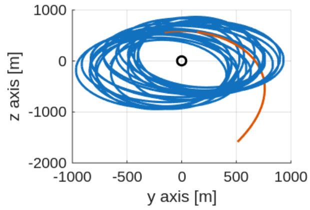

(f) B, yz plane

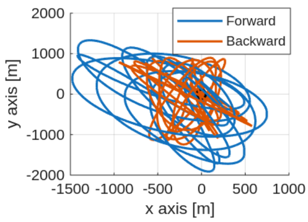

(g) C, xy plane

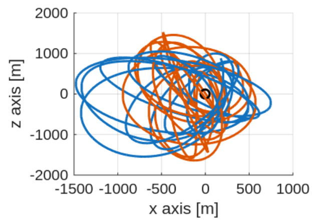

(h) C, xz plane

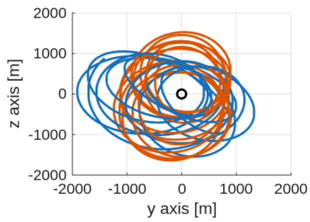

(i) C, yz plane

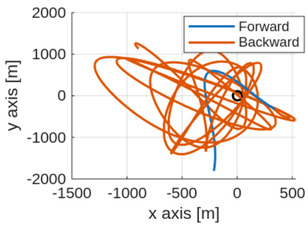

(j) D, xy plane

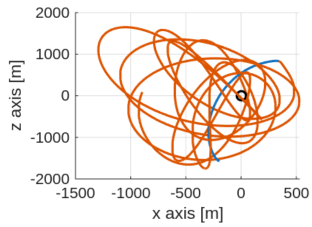

(k) D, xz plane

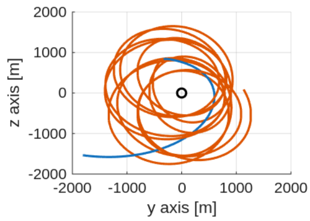

(l) D, yz plane

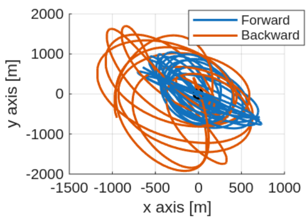

(m) E, xy plane

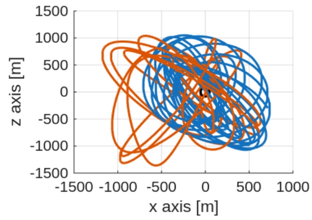

(n) E, xz plane

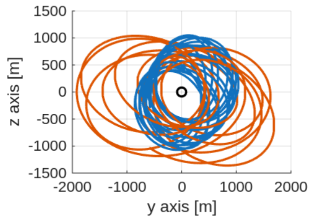

(o) E, yz plane

Figure 5.6: $(\alpha = 0°, \theta = 100°)$ and $(\alpha = 10°, \theta = 110°)$ sample trajectories.

Figure 5.7 shows the regions ($\alpha = 0°, \theta = -50°$) and ($\alpha = -10°, \theta = -60°$). The detected structures resemble the behaviour of the last ones, where changing the angle α increases the bounded trajectories. The sampled trajectories are shown in Figure 5.8. The detected LD structures capture the qualitative behaviour except for trajectory K, where the trajectory escapes Apophis in forward time. This is caused by the considered integration time, in fact the forward branch of the trajectory escapes Apophis near the end of the considered time window, and the LD method would require a higher integration time to detect this different behaviour. It is also noticed that the case ($\alpha = -10°, \theta = -60°$) shows a significantly small region of bounded backward trajectories, and the sampled trajectory I shows approximately the same distance with respect to Apophis in both forward and backward time branches.

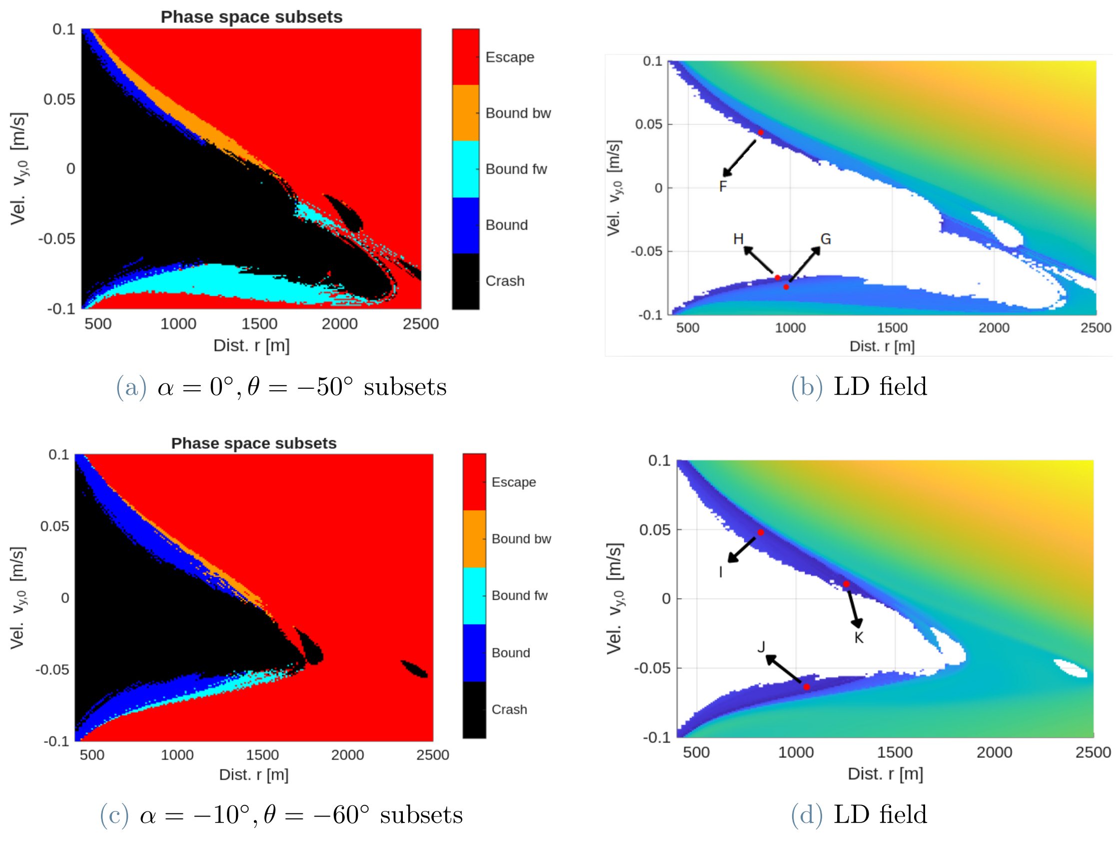

(a) $\alpha = 0°, \theta = -50°$ subsets

(b) LD field

(c) $\alpha = -10°, \theta = -60°$ subsets

(d) LD field

Figure 5.7: ($\alpha = 0°, \theta = -50°$) and ($\alpha = -10°, \theta = -60°$) subsets and LD fields.

ID	x [m]	y [m]	z [m]	v_x [m/s]	v_y [m/s]	v_z [m/s]	Motion
F	-485	21.5	-702	0.0176	-0.0377	-0.0133	Bounded
G	-557	24.7	-806	-0.0314	0.0672	0.0238	Bounded forward
H	-533	23.7	-771	-0.0286	0.0611	0.0216	Bounded
I	-410	214	-680	0.0192	-0.0412	-0.0146	Bounded
J	-526	275	-872	-0.0257	0.0551	0.0195	Bounded
K	-626	327	-1037	0.0043	-0.0091	-0.0032	Bounded backward

Table 5.2: Initial states, at Earth CE, of considered trajectories in Apophis centered J2000 reference frame for $(\alpha = 0°, \theta = -50°)$ and $(\alpha = -10°, \theta = -60°)$.

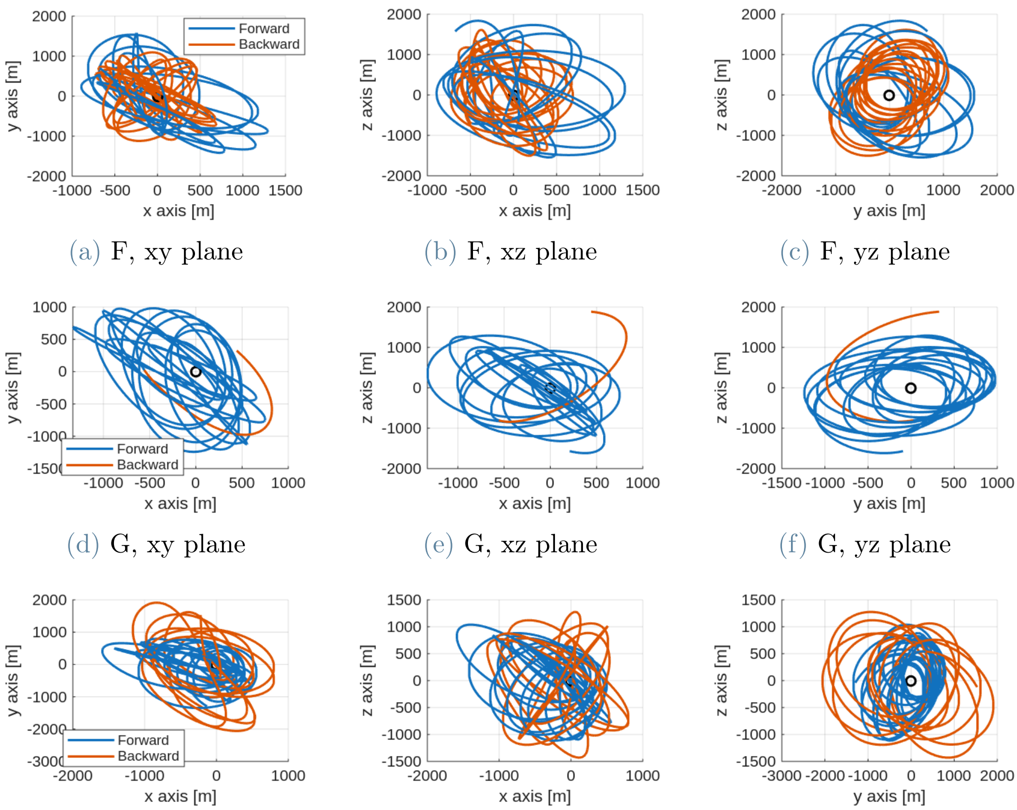

(a) F, xy plane (b) F, xz plane (c) F, yz plane

(d) G, xy plane (e) G, xz plane (f) G, yz plane

(g) H, xy plane (h) H, xz plane (i) H, yz plane

Figure 5.8: $(\alpha = 0°, \theta = -50°)$ and $(\alpha = -10°, \theta = -60°)$ sample trajectories (part I).

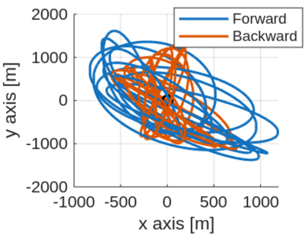

(j) I, xy plane

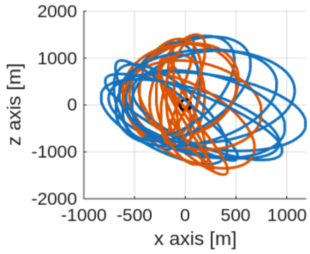

(k) I, xz plane

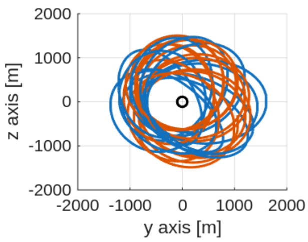

(l) I, yz plane

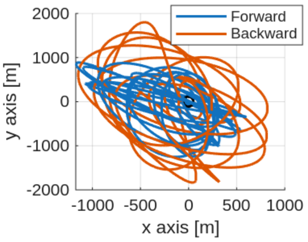

(m) J, xy plane

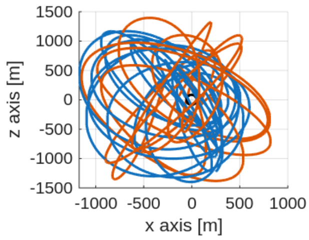

(n) J, xz plane

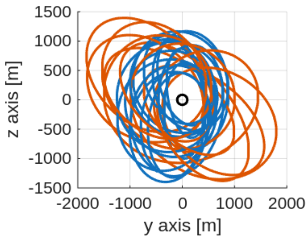

(o) J, yz plane

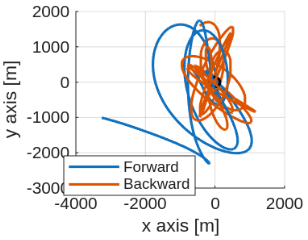

(p) K, xy plane

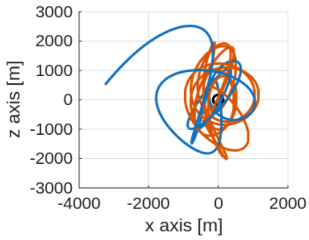

(q) K, xz plane

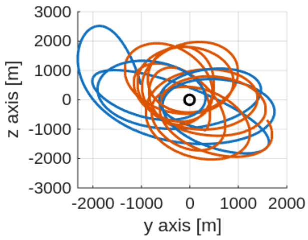

(r) K, yz plane

Figure 5.8: ($\alpha = 0°, \theta = -50°$) and ($\alpha = -10°, \theta = -60°$) sample trajectories (part II).

Integration errors

As mentioned in subsection 3.2.3, it is necessary to evaluate the error in the final state due to the selected low-order integrator. To compare the results, the final position vector is compared with the final position vector of the 9^{th} order variable step Runge-Kutta MATLAB integrator. The selected cases to compare the final position are ($\alpha = 10°, \theta = 110°$) and ($\alpha = -10°, \theta = -60°$), considering initial time t_{CE} and final time 18 days later. From Figure 5.9, it is noticed that the error is acceptable in the majority of the considered initial conditions. The impact condition causes errors on the order of meters: the MATLAB integrator finds the precise instant of impact, whereas the GPU integrator stops the integration at the end of the timestep at which the impact occurs. Regions with high position error are caused by trajectories that pass through Apophis shadow cylinder. The low-order integrator cannot capture the full dynamics of these trajectories, however the qualitative behaviour of the trajectory is still captured, signaling an escaped trajectory in either case.

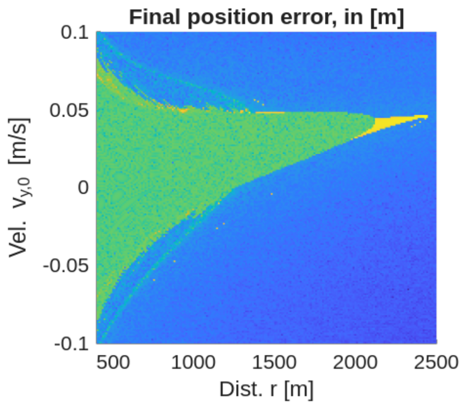

(s) $\alpha = 10°, \theta = 110°$

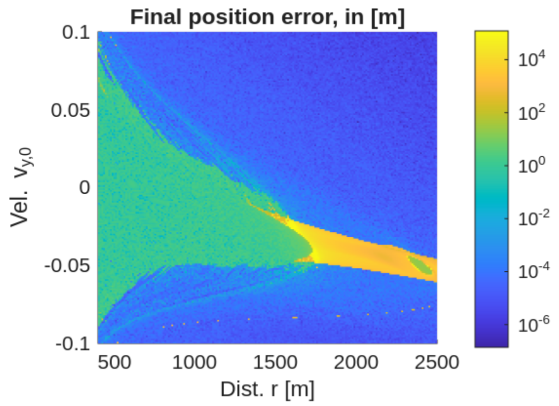

(t) $\alpha = -10°, \theta = -60°$

Figure 5.9: GPU error on final position in logarithmic scale, considering MATLAB 9^{th} order integrator as baseline.

5.2.1. Farinella navigation constraints

Now that regions of bounded motion have been identified, their characteristics are evaluated, specifically considering the evolution of the phase angle and Apophis range. The sampled orbits are evaluated considering the constraints in subsection 2.1.3. Figure 5.10 reports both range and phase angle evolution over the considered time window $t_{CE} \pm 18$ days. It is noticed that some samples share characteristics with RTO: trajectories A, C, E, and J show resemblance to dark-side RTO, with some cases showing these characteristics only before or after Apophis CE; and trajectories F and I show Sun-side RTO similarities, the last one both before and after the CE. Considering Farinella constraints, Sun-side RTO are preferred since Apophis will be visible at each ellipse apoapsis, which is above 1.4 km in some cases. Dark-side RTO, on the other hand, spends the majority of the time with Apophis not visible. It is also highlighted that the considered couple of angles (α, θ) determine the visibility of Apophis at the CE: with $(\alpha, \theta) = (0°, 100°), (10°, 110°)$ Apophis is visible in the considered epoch; and with $(\alpha, \theta) = (0°, -50°), (-10°, -60°)$ Apophis is not visible. Among all sampled trajectories, F and I are the most promising.

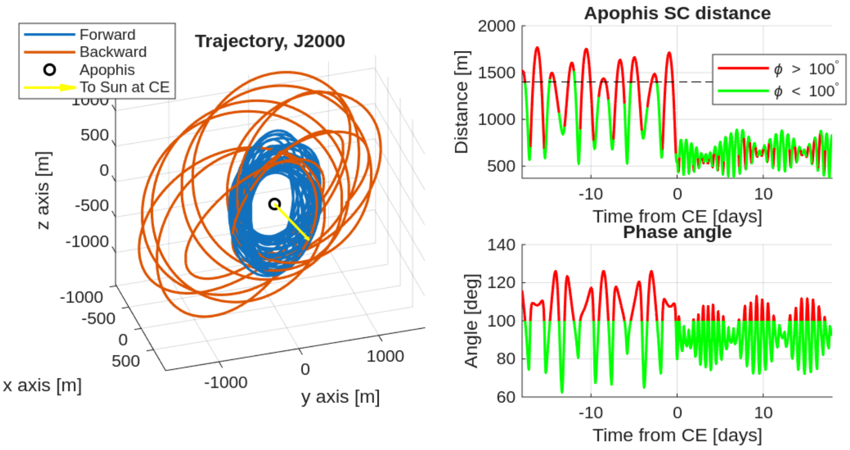

(a) Trajectory A

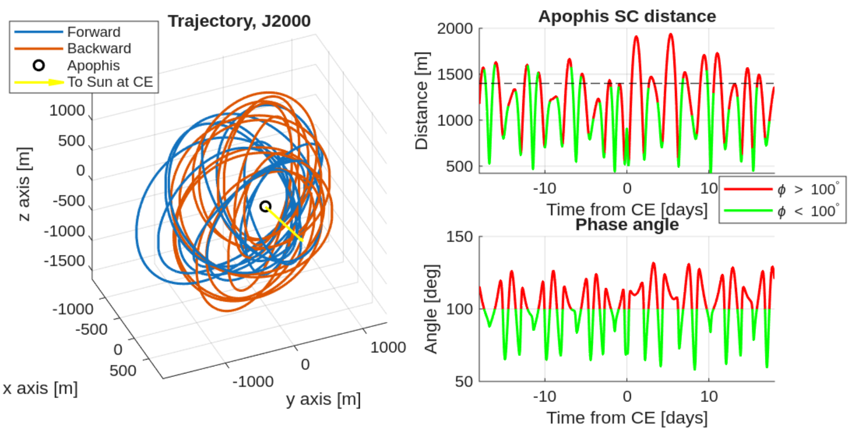

(b) Trajectory C

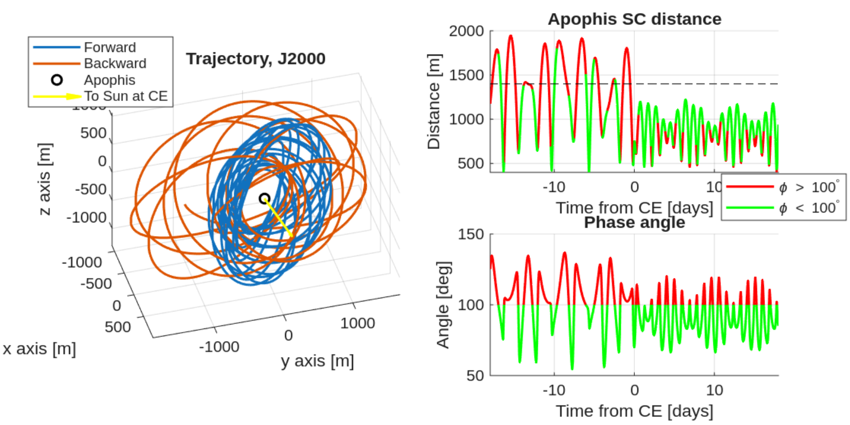

(c) Trajectory E

Figure 5.10: Sampled trajectories range and phase angle (part I).

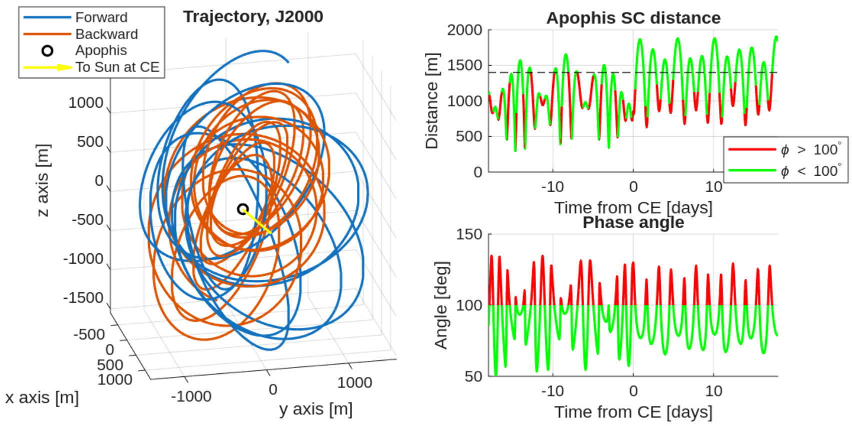

(d) Trajectory F

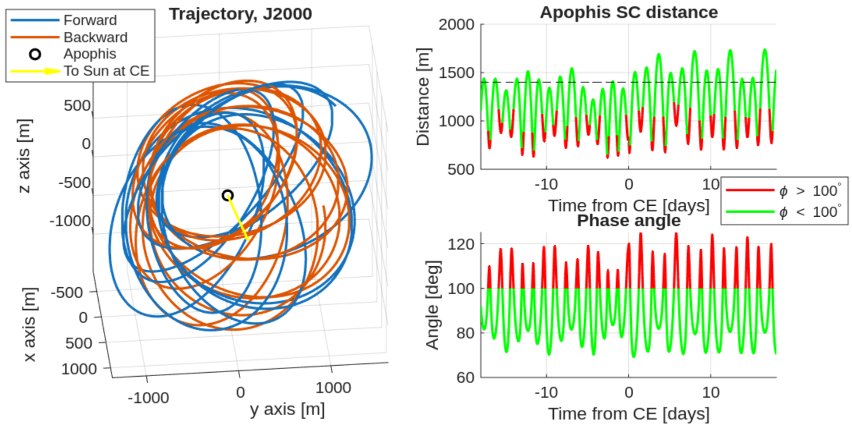

(e) Trajectory I

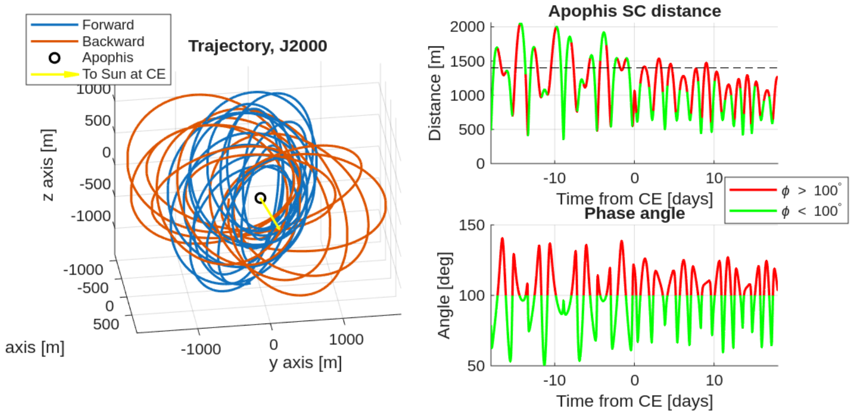

(f) Trajectory J

Figure 5.10: Sampled trajectories range and phase angle (part II).

6 | Conclusions

This thesis presents a numerical investigation into the dynamical environment in the proximity of asteroid (99942) Apophis during its 2029 Earth close approach. This chapter summarizes the key findings while also proposing potential future works.

Thesis objectives

Find regions of bounded motion around Apophis during its close encounter with the Earth

Regions of bounded motion are found by firstly reducing the dimensionality of the problem, defining an osculating Hill reference frame at Apophis close encounter with the Earth and exploiting the peculiar geometry of the flyby. Afterward, several grids of initial states are defined and numerically propagated using a GPU enhanced integrator, bounded trajectories are then detected and counted. With this procedure, several regions of bounded motion are identified and then studied with the use of Lagrangian descriptors.

The use of GPU parallelization methods significantly reduces the time required to evaluate all initial states, and the error introduced by considering a low order integrator is acceptable for the majority of the considered initial states. When the propagation error is not acceptable, the qualitative characteristic of the trajectory is still retained.

Investigate the capability of different Lagrangian descriptors to reveal organizing structures in non-autonomous astrodynamics systems

Once regions with bounded motion are found, Lagrangian descriptors are applied. The capability of Lagrangian descriptors to reveal underlying dynamical structures depends on both the considered propagation time and Lagrangian descriptor choice. Velocity related LD shows better performances, the positive quantity defined in Table 4.1 shows acceptable results, while acceleration related LD cannot detect the dynamical structures. Cases where the selected LD fails are also found, and it is supposed that they depend on the selected integration time.

Assess the feasibility of bounded orbits in relation to Farinella navigation constraints

Most bounded motion shows, before or after the CE, characteristics analogous to terminator orbits, and both Sun-side and Dark-side RTO. With the considered navigation constraints, Sun-side RTO shows the most promising characteristics, with Apophis visible for large interval of times, and briefly at distances above 1.4 km.

Research question

To what extent do Lagrangian Descriptors provide insight into the Apophis dynamical environment at the close approach with the Earth by revealing the structures that organize the phase space into regions of different behavior?

LD proves to be effective in unveiling underlying dynamical structures for this specific problem, and provides clear distinctions between qualitatively different trajectories, such as cases where the cubesat escapes Apophis in both forward and backward time, only one of the two branches, or if the motion stays in Apophis neighborhood. Furthermore, the asteroid visibility at the Earth CE depends on the selected bounded region.

Future works

This thesis present several assumptions in the description of Apophis, the most important ones being the total mass and its spin state evolution. Recent estimation of Apophis total mass present a wide range of uncertainties, therefore one value is selected and assumed true. Apophis spin state also present uncertainties, and they heavily influence the knowledge of the spin state evolution during and after the Earth flyby. Once these uncertainties are reduced, the bounded trajectories should be evaluated again to verify that they retain the characteristics highlighted in this work.

Bounded trajectories that satisfy Farinella navigation constraints are detected, however the sensitivity to initial conditions is not considered. This should be assessed in future works if Farinella should employ one of the presented trajectories. In addition to this, navigation errors with optical based state estimation should be estimated considering the brief time intervals where Apophis do not saturate the camera field of view, and thus evaluate the feasibility of the proposed trajectories. Lastly, the scientific return should also be estimated, considering both camera image resolution and radar measurements.

Lastly, the dimensionality reduction strategy effectively cuts out a large part of the total phase space, and additional strategies can be evaluated to fully characterize the entirety of the phase space.

Bibliography

[1] C. H. Acton. Ancillary data services of nasa's navigation and ancillary information facility. *Planetary and Space Science*, 44(1):65–70, 1996. ISSN 0032-0633. doi: https://doi.org/10.1016/0032-0633(95)00107-7. URL `https://www.sciencedirect.com/science/article/pii/0032063395001077`. Planetary data system.

[2] G. Azzola. A study on the mission design for milani cubesat to apophis. Master's thesis, Politecnico di Milano, https://hdl.handle.net/10589/231449, 12 2024.

[3] C. J. Benson, D. J. Scheeres, M. Brozović, et al. Spin state evolution of (99942) apophis during its 2029 earth encounter. *Icarus*, 390:115324, 2023. ISSN 0019-1035. doi: https://doi.org/10.1016/j.icarus.2022.115324. URL `https://www.sciencedirect.com/science/article/pii/S001910352200416X`.

[4] R. Binzel et al. Apophis 2029: Decadal Opportunity for the Science of Planetary Defense. *Bulletin of the AAS*, 53(4), mar 18 2021. https://baas.aas.org/pub/2021n4i045.

[5] S. B. Broschart, G. Lantoine, and D. J. Grebow. Quasi-terminator orbits near primitive bodies. *Celestial Mechanics and Dynamical Astronomy*, 120(2):195–215, October 2014. doi: 10.1007/s10569-014-9574-3. URL `https://doi.org/10.1007/s10569-014-9574-3`.

[6] G. M. Brown, D. R. Wibben, P. G. Antreasian, and K. M. Getzandanner. Leveraging resonant terminator orbits for the trajectory design of OSIRIS-APEX at (99942) Apophis. In *46th Annual AAS Guidance, Navigation and Control Conference*, Breckenridge, CO, February 2024. URL `https://ntrs.nasa.gov/citations/20240000812`.

[7] M. Brozović et al. Goldstone and arecibo radar observations of (99942) apophis in 2012–2013. *Icarus*, 300:115–128, 2018. ISSN 0019-1035. doi: https://doi.org/10.1016/j.icarus.2017.08.032. URL `https://www.sciencedirect.com/science/article/pii/S0019103517302865`.

[8] D. Canales and K. Howell. Understanding flow around planetary moons via finite-time lyapunov exponent maps. *Celestial Mechanics and Dynamical Astronomy*, 136

(5):40, 2024. doi: 10.1007/s10569-024-10213-3. URL https://doi.org/10.1007/s10569-024-10213-3.

[9] J. A. Christian, L. Hong, P. McKee, R. Christensen, and T. P. Crain. Image-based lunar terrain relative navigation without a map: Measurements. *Journal of Spacecraft and Rockets*, 58(1):164–181, 2021. doi: 10.2514/1.A34875. URL https://doi.org/10.2514/1.A34875.

[10] L. E. Cunningham. On the computation of the spherical harmonic terms needed during the numerical integration of the orbital motion of an artificial satellite. *Celestial Mechanics*, 2(2):207–216, June 1970. doi: 10.1007/BF01229495. URL https://doi.org/10.1007/BF01229495.

[11] H. D. Curtis. Chapter 2 - the two-body problem. In H. D. Curtis, editor, *Orbital Mechanics for Engineering Students (Third Edition)*, pages 59–144. Butterworth-Heinemann, Boston, third edition edition, 2014. ISBN 978-0-08-097747-8. doi: https://doi.org/10.1016/B978-0-08-097747-8.00002-5. URL https://www.sciencedirect.com/science/article/pii/B9780080977478000025.

[12] H. Dankowicz. Some special orbits in the two-body problem with radiation pressure. *Celestial Mechanics and Dynamical Astronomy*, 58(4):353–370, 1994. doi: 10.1007/BF00692010. URL https://doi.org/10.1007/BF00692010.

[13] D. N. DellaGiustina et al. Osiris-apex: An osiris-rex extended mission to asteroid apophis. *The Planetary Science Journal*, 4(10):198, oct 2023. doi: 10.3847/PSJ/acf75e. URL https://doi.org/10.3847/PSJ/acf75e.

[14] J. Dormand and P. Prince. A family of embedded runge-kutta formulae. *Journal of Computational and Applied Mathematics*, 6(1):19–26, 1980. ISSN 0377-0427. doi: https://doi.org/10.1016/0771-050X(80)90013-3. URL https://www.sciencedirect.com/science/article/pii/0771050X80900133.

[15] E. Dotto et al. Liciacube - the light italian cubesat for imaging of asteroids in support of the nasa dart mission towards asteroid (65803) didymos. *Planetary and Space Science*, 199:105185, 2021. ISSN 0032-0633. doi: https://doi.org/10.1016/j.pss.2021.105185. URL https://www.sciencedirect.com/science/article/pii/S0032063321000246.

[16] M. Farazmand and G. Haller. Erratum and addendum to “a variational theory of hyperbolic lagrangian coherent structures” [physica d 240 (2011) 574–598]. *Physica D: Nonlinear Phenomena*, 241(4):439–441, 2012. ISSN 0167-2789. doi:

https://doi.org/10.1016/j.physd.2011.09.013. URL https://www.sciencedirect.com/science/article/pii/S0167278911002600.

[17] M. Farazmand and G. Haller. Computing lagrangian coherent structures from their variational theory. *Chaos: An Interdisciplinary Journal of Nonlinear Science*, 22(1): 013128, 03 2012. ISSN 1054-1500. doi: 10.1063/1.3690153. URL https://doi.org/10.1063/1.3690153.

[18] D. Farnocchia, S. Chesley, P. Chodas, M. Micheli, D. Tholen, A. Milani, G. Elliott, and F. Bernardi. Yarkovsky-driven impact risk analysis for asteroid (99942) apophis. *Icarus*, 224(1):192–200, 2013. ISSN 0019-1035. doi: https://doi.org/10.1016/j.icarus.2013.02.020. URL https://www.sciencedirect.com/science/article/pii/S0019103513000821.

[19] E. S. Gawlik, J. E. Marsden, P. C. Du Toit, and S. Campagnola. Lagrangian coherent structures in the planar elliptic restricted three-body problem. *Celestial Mechanics and Dynamical Astronomy*, 103(3):227–249, 2009. doi: 10.1007/s10569-008-9180-3. URL https://doi.org/10.1007/s10569-008-9180-3.

[20] M. Geda. Massive parallelization of trajectory propagations using gpus. Master's thesis, TU Delft, https://repository.tudelft.nl/record/uuid:1db3f2d1-c2bb-4188-bd1e-dac67bfd9dab, 2019.

[21] M. Giancotti. *Stable orbits in the proximity of an asteroid: solutions for the Hayabusa 2 mission*. PhD thesis, Università degli Studi di Roma La Sapienza, https://hdl.handle.net/20.500.14242/91717, 02 2014.

[22] J. D. Giorgini, D. K. Yeomans, A. B. Chamberlin, P. W. Chodas, R. A. Jacobson, M. S. Keesey, J. H. Lieske, S. J. Ostro, E. M. Standish, and R. N. Wimberly. JPL's On-Line Solar System Data Service, 1996. URL https://hdl.handle.net/2014/27350.

[23] G. Haller. A variational theory of hyperbolic lagrangian coherent structures. *Physica D: Nonlinear Phenomena*, 240(7):574–598, 2011. ISSN 0167-2789. doi: https://doi.org/10.1016/j.physd.2010.11.010. URL https://www.sciencedirect.com/science/article/pii/S0167278910003143.

[24] K. C. Howell. Three-dimensional, periodic, 'halo' orbits. *Celestial Mechanics*, 32 (1):53–71, Jan 1984. doi: 10.1007/BF01358403. URL https://doi.org/10.1007/BF01358403.

[25] W. S. Koon, M. W. Lo, J. E. Marsden, and S. D. Ross. *Dynamical Systems, the*

Three-Body Problem and Space Mission Design. Marsden Books, 2022. ISBN 978-0-615-24095-4. URL `https://ross.aoe.vt.edu/books/`.

[26] M. Küppers, P. Martino, I. Carnelli, and P. Michel. Rapid Apophis mission for space safety (RAMSES) – ESA's study to rendezvous Apophis during its flyby of Earth. In *55th Lunar and Planetary Science Conference*, page 1087, The Woodlands, Texas, March 2024. URL `https://hal.science/hal-04782390`. Abstract 1087.

[27] A. M. Mancho, S. Wiggins, J. Curbelo, and C. Mendoza. Lagrangian descriptors: A method for revealing phase space structures of general time dependent dynamical systems. *Communications in Nonlinear Science and Numerical Simulation*, 18(12):3530–3557, 2013. ISSN 1007-5704. doi: https://doi.org/10.1016/j.cnsns.2013.05.002. URL `https://www.sciencedirect.com/science/article/pii/S1007570413002037`.

[28] C. Mendoza and A. M. Mancho. Hidden geometry of ocean flows. *Phys. Rev. Lett.*, 105:038501, Jul 2010. doi: 10.1103/PhysRevLett.105.038501. URL `https://link.aps.org/doi/10.1103/PhysRevLett.105.038501`.

[29] P. Michel et al. The esa hera mission: Detailed characterization of the dart impact outcome and of the binary asteroid (65803) didymos. *The Planetary Science Journal*, 3(7):160, jul 2022. doi: 10.3847/PSJ/ac6f52. URL `https://doi.org/10.3847/PSJ/ac6f52`.

[30] P. Pravec et al. The tumbling spin state of (99942) apophis. *Icarus*, 233:48–60, 2014. ISSN 0019-1035. doi: https://doi.org/10.1016/j.icarus.2014.01.026. URL `https://www.sciencedirect.com/science/article/pii/S0019103514000578`.

[31] M. Pugliatti, F. Piccolo, A. Rizza, V. Franzese, and F. Topputo. The vision-based guidance, navigation, and control system of hera's milani cubesat. *Acta Astronautica*, 210:14–28, 2023. ISSN 0094-5765. doi: https://doi.org/10.1016/j.actaastro.2023.04.047. URL `https://www.sciencedirect.com/science/article/pii/S0094576523002205`.

[32] A. Quinci. Qualitative study of ballistic capture at mars via lagrangian descriptors. Master's thesis, Politecnico di Milano, https://hdl.handle.net/10589/186116, 4 2022.

[33] S. Raffa. Finding regions of bounded motion in binary asteroid environments using lagrangian descriptors. Master's thesis, Politecnico di Milano, https://hdl.handle.net/10589/186129, 4 2022.

[34] D. J. Scheeres. Proximity operations about apophis through its 2029 earth flyby.

The Journal of the Astronautical Sciences, 69(6):1514–1536, Dec 2022. doi: 10.1007/s40295-022-00360-w. URL `https://doi.org/10.1007/s40295-022-00360-w`.

[35] S. C. Shadden, F. Lekien, and J. E. Marsden. Definition and properties of lagrangian coherent structures from finite-time lyapunov exponents in two-dimensional aperiodic flows. *Physica D: Nonlinear Phenomena*, 212(3):271–304, 2005. ISSN 0167-2789. doi: https://doi.org/10.1016/j.physd.2005.10.007. URL `https://www.sciencedirect.com/science/article/pii/S0167278905004446`.

[36] C. Simó and T. Stuchi. Central stable/unstable manifolds and the destruction of kam tori in the planar hill problem. *Physica D: Nonlinear Phenomena*, 140(1):1–32, 2000. ISSN 0167-2789. doi: https://doi.org/10.1016/S0167-2789(99)00211-0. URL `https://www.sciencedirect.com/science/article/pii/S0167278999002110`.

[37] S. Takahashi and D. J. Scheeres. Higher-order corrections for frozen terminator orbit design. *Journal of Guidance, Control, and Dynamics*, 43(9):1642–1655, 2020. doi: 10.2514/1.G004901. URL `https://doi.org/10.2514/1.G004901`.

[38] G. Valvano, O. C. Winter, R. Sfair, R. Machado Oliveira, G. Borderes-Motta, and T. S. Moura. Apophis – effects of the 2029 earth's encounter on the surface and nearby dynamics. *Monthly Notices of the Royal Astronomical Society*, 510(1):95–109, 11 2021. ISSN 0035-8711. doi: 10.1093/mnras/stab3299. URL `https://doi.org/10.1093/mnras/stab3299`.

[39] R. A. Werner. The gravitational potential of a homogeneous polyhedron or don't cut corners. *Celestial Mechanics and Dynamical Astronomy*, 59(3):253–278, July 1994. doi: 10.1007/BF00692875. URL `https://doi.org/10.1007/BF00692875`.

[40] R. A. Werner. Spherical harmonic coefficients for the potential of a constant-density polyhedron. *Computers Geosciences*, 23(10):1071–1077, 1997. ISSN 0098-3004. doi: https://doi.org/10.1016/S0098-3004(97)00110-6. URL `https://www.sciencedirect.com/science/article/pii/S0098300497001106`.

[41] R. A. Werner and D. J. Scheeres. Exterior gravitation of a polyhedron derived and compared with harmonic and mascon gravitation representations of asteroid 4769 castalia. *Celestial Mechanics and Dynamical Astronomy*, 65(3):313–344, September 1996. doi: 10.1007/BF00053511. URL `https://doi.org/10.1007/BF00053511`.

A | Polyhedron model

Below a summary of the method presented in [39, 41] is reported. Given a polyhedron model and the total mass of the central body, the gravitational acceleration is computed as:

$$\boldsymbol{a}_b = -G\rho \left(\sum_{e \in \text{edges}} \boldsymbol{E}_e \cdot \boldsymbol{r}_e L_e - \sum_{f \in \text{faces}} \boldsymbol{F}_f \cdot \boldsymbol{r}_f \omega_f \right) \tag{A.1}$$

where G is the universal constant of gravitation, ρ is the bulk density computed according to the assumed mass and polyhedron volume, $\boldsymbol{r}_e$ and $\boldsymbol{r}_f$ are the vectors from the considered field point to any point of the edge e and face f, respectively. The face dyad $\boldsymbol{F}_e$ is obtained as:

$$\boldsymbol{F}_f = \hat{\boldsymbol{n}}_A \otimes \hat{\boldsymbol{n}}_A$$

while the edge dyad is defined as:

$$\boldsymbol{E}_e = \hat{\boldsymbol{n}}_A \otimes \hat{\boldsymbol{n}}_{12}^A + \hat{\boldsymbol{n}}_B \otimes \hat{\boldsymbol{n}}_{21}^B$$

where the considered edge is shared by faces A and B and vertices 1 and 2, and $\otimes$ represent the cross product operation between vectors. The normal to the considered face is always outward with respect to the center of the polyhedron, as in Figure A.1a. The edge normals are defined as $\hat{\boldsymbol{n}}_{12}^A = P_1P_2 \times \hat{\boldsymbol{n}}_A$ and $\hat{\boldsymbol{n}}_{21}^B = P_2P_1 \times \hat{\boldsymbol{n}}_B$ as in Figure A.1b.

Finally, the solid angle associated with the face f is:

$$\omega_f = 2 \arctan \left(\frac{\boldsymbol{r}_i \cdot \boldsymbol{r}_j \times \boldsymbol{r}_k}{r_i r_j r_k + r_i(\boldsymbol{r}_j \cdot \boldsymbol{r}_k) + r_k(\boldsymbol{r}_j \cdot \boldsymbol{r}_i)} \right)$$

where $\boldsymbol{r}_i,\ \boldsymbol{r}_j,\ \boldsymbol{r}_k$ are the distances of the face vertices with respect to the considered field point. The potential of a wire L_e is then defined as:

$$L_e = \ln \frac{r_i + r_j + l}{r_i + r_j - l}$$

where $l = ||\boldsymbol{r}_2 - \boldsymbol{r}_1||$ is the edge length.

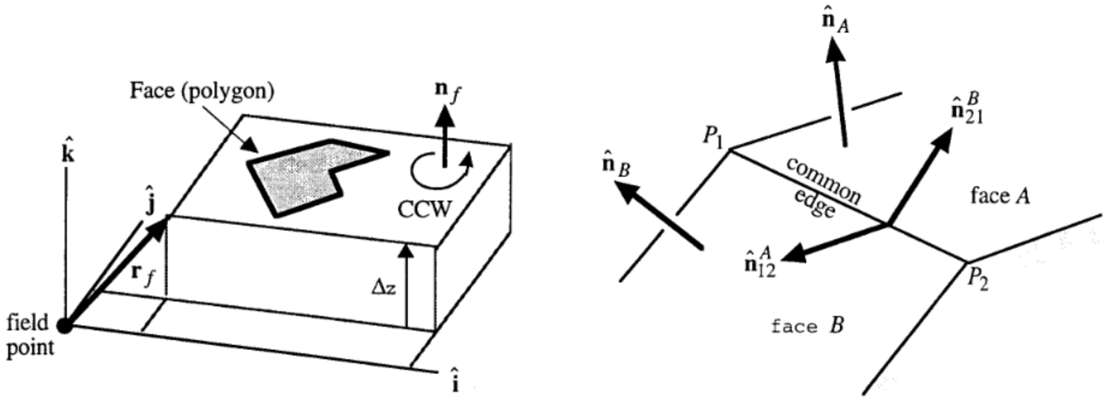

(a) Face normal definition.

(b) Edge normal definitions.

Figure A.1: Definition of (a) face normal and (b) edge normals, image from [41].

List of Figures

List of Tables

List of Abbreviations

ESA European Space Agency

NASA National Aeronautics and Space Administration

RAMSES Rapid Apophis Mission for Space Safety

CE Close Encounter

SRP Solar Radiation Pressure

LCS Lagrangian Coherent Structures

STM State Transition Matrix

LD Lagrangian Descriptors

CRTBP Circular Restricted Three Body Problem

RTO Resonant Terminator Orbit

FTLE Finite Time Lyapunov Exponent

Acknowledgements

Alla fine di questo percorso, mi sento di ringraziare delle persone a me importanti.

Desidero ringraziare innanzitutto il Prof. Topputo e i miei co-relatori per i validi consigli e per l'opportunitá che mi hanno dato.

Ringrazio i miei genitori, le mie persone di riferimento, per avermi sempre incoraggiato e supportato, questo traguardo sarebbe stato impossibile senza il loro continuo sostegno.

Ringrazio la mia famiglia, per essermi sempre stata affianco durante questo percorso nonostante tutto.

Particolari ringraziamenti vanno a Giorgia, per avermi supportato incondizionatamente e creduto in me piú di quanto facessi io stesso. La tua sola presenza ha reso il mio percorso molto più felice.

Ultimi, ma non per importanza, ringrazio Lorenzo, Riccardo, Alessandro e Matteo, per aver portato leggerezza e allegria durante le lunghe ore passate a studiare assieme.